Hopping and the Stokes–Einstein relation breakdown in simple glass formers

Patrick Charbonneau
Departments of Chemistry and Physics, Duke University, Durham, North Carolina 27708, USA

Yuliang Jin
Departments of Chemistry and Physics, Duke University, Durham, North Carolina 27708, USA and
Dipartimento di Fisica, Sapienza Universitá di Roma, INFN,
Sezione di Roma I, IPFC – CNR, P.le A. Moro 2, I-00185 Roma, Italy

Giorgio Parisi
Dipartimento di Fisica, Sapienza Università di Roma, INFN,
Sezione di Roma I, IPFC – CNR, P.le A. Moro 2, I-00185 Roma, Italy

Francesco Zamponi
LPT, École Normale Supérieure, UMR 8549 CNRS, 24 Rue Lhomond, 75005 France

arXiv:1407.5677v2 [cond-mat.dis-nn] 15 Sep 2014

One of the most actively debated issues in the study of the glass transition is whether a mean-field description is a reasonable starting point for understanding experimental glass formers. Although the mean-field theory of the glass transition – like that of other statistical systems – is exact when the spatial dimension $d \to \infty$, the evolution of systems properties with d may not be smooth. Finite-dimensional effects could dramatically change what happens in physical dimensions, $d = 2, 3$. For standard phase transitions finite-dimensional effects are typically captured by renormalization group methods, but for glasses the corrections are much more subtle and only partially understood. Here, we investigate hopping between localized cages formed by neighboring particles in a model that allows to cleanly isolate that effect. By bringing together results from replica theory, cavity reconstruction, void percolation, and molecular dynamics, we obtain insights into how hopping induces a breakdown of the Stokes–Einstein relation and modifies the mean-field scenario in experimental systems. Although hopping is found to supersede the dynamical glass transition, it nonetheless leaves a sizable part of the critical regime untouched. By providing a constructive framework for identifying and quantifying the role of hopping, we thus take an important step towards describing dynamic facilitation in the framework of the mean-field theory of glasses.

Significance Like crystals, glasses are rigid because of the *self-caging* of their constituent particles. The key difference is that crystal formation is a sharp first order phase transition at which cages form abruptly and remain stable, while glass formation entails the progressive emergence of cages. This loose caging complicates the description of the glass transition. In particular, an important transport mechanism in this regime, hopping, has thus far been difficult to characterize. Here we develop a completely microscopic description of hopping, which allows us to clearly assess its impact on transport anomalies, such as the breakdown of the Stokes–Einstein relation.

Introduction - Glasses are amorphous materials whose rigidity emerges from the mutual caging of their constituent particles – be they atoms, molecules, colloids, grains, or cells. Although glasses are ubiquitous, the microscopic description of their formation, rheology, and other dynamical features is still far from satisfying. Developing a more complete theoretical framework would not only resolve epistemological wrangles [1], but also improve our material control and design capabilities. Yet such a research program remains fraught with challenges. Conventional paradigms based on perturbative expansions around the low-density, ideal gas limit (for moderately dense gases and liquids), or on harmonic expansions around an ideal lattice (for crystals) fail badly. Because dense amorphous materials interact strongly, low-density expansions are unreliable, while harmonic expansions lack reference equilibrium particle positions. These fundamental difficulties must somehow be surmounted in order to describe the dynamical processes at play in glass formation.

A celebrated strategy for studying phase transitions is to consider first their mean-field description, which becomes exact when the spatial dimension d of the system goes to infinity [2], before including corrections to this description. In that spirit, we open with the $d \to \infty$ "ideal" random first-order transition (iRFOT) scenario, which, based on the analysis of simple models, brings together static- [3–5] and dynamics-based (mode-coupling) [6] results for glass formation (see, e.g., [7, 8] for reviews) [8–11]. In iRFOT, an infinitely slowly cooled simple liquid (or compressed hard sphere fluid) becomes infinitely viscous, i.e., forms a glass in which particles are completely caged, at the (critical) dynamical transition temperature T_d (or packing fraction φ_d). Upon approaching this transition, caging makes the diffusivity D vanish as a power-law $D \sim (T - T_\mathrm{d})^\gamma$, and the viscosity diverge as $\eta \sim (T - T_\mathrm{d})^{-\gamma}$. Hence, in the critical regime one ex-

pects the Stokes–Einstein relation (SER) between transport coefficients, $D \sim \eta^{-1}$, to hold. In short, the $d \to \infty$ scenario is characterized by (i) a sharp dynamical glass transition associated with perfect caging, (ii) a power-law divergence of η, and (iii) the SER being obeyed.

As observed in Ref. [12], the phenomenology of finite-dimensional systems is, however, quite different from the iRFOT scenario. In particular, it does not recapitulate elementary experimental observations, such as Vogel-Tammann-Fulcher (VTF) viscosity scaling in fragile glasses, $\eta \sim e^{B_{\rm VTF}/(T-T_0)}$ ($B_{\rm VTF}$ and T_0 are phenomenological constants), and breakdown of the SER, $D \sim \eta^{-1+\omega}$ (phenomenologically $\omega > 0$) [13–16]. As a result, the relevance of the iRFOT picture for experimental systems remains the object of lively debates.

Part of the difficulty of clarifying the situation in finite d, where the iRFOT description is only approximate and the dynamical transition is but a crossover, lies in the shear number of different contributions one has to take into account. From a purely field-theoretic point of view, one has to include finite-dimensional corrections to critical fluctuations. A Ginzburg criterion gives $d_u = 8$ as the upper critical dimension for the dynamical transition [17–20], and hence for $d < d_u$ critical fluctuations renormalize the power-law scaling exponents. In principle, these corrections could be captured by a perturbative $d_u - d$ expansion, and phenomenological arguments along this direction indicate that they could also induce a SER breakdown [17]. A number of non-perturbative processes in $1/d$ must additionally be considered. (i) In the iRFOT picture, caging is perfect, hence in the glass phase each particle is forever confined to a finite region of space delimited by its neighbors [6]. However, it has been theoretically proven [21] and experimentally observed [22] that in low-dimensional systems the diffusivity is never strictly zero. Single particles can indeed hop between neighboring cages [23–26], and the free space they leave behind can *facilitate* the hopping of neighboring particles. Facilitation can thus result in cooperative hopping and avalanche formation [27–29]. (ii) For some glass formers, activated crystal nucleation cannot be neglected and interferes with the dynamical arrest, leading to a glass composed of microscopic geometrically frustrated crystal domains [30]. (iii) In the iRFOT scenario, the dynamical arrest is related to the emergence of a huge number of distinct metastable glass states whose lifetime is infinite. In finite dimensions, however, a complex glass-glass nucleation process gives a finite lifetime to these metastable states [5, 12, 31]. The dynamics of glass-forming liquids is then profoundly affected. Including glass-glass nucleation into iRFOT leads to the complete RFOT scenario [12], in which the mean-field dynamical glass transition becomes but a crossover [12], and both VTF scaling and facilitation are recovered [32, 33].

Because the treatment of these different processes has thus far been mostly qualitative, their relative importance cannot be easily evaluated. A controlled first-principle, *quantitative* treatment is for the moment limited to the exact solution for $d \to \infty$ [10, 11, 34, 35]. Its approximate extension to finite d [6, 8, 36] completely ignores the non-perturbative effects mentioned above. This approach therefore cannot, on its own, cleanly disentangle the various corrections. Systematic studies of glass formation as a function of d have encouragingly shown that these corrections are limited, even down to $d = 3$ [15, 16, 37–40], provided length and time scales are not too large, as is typical of numerical simulations and experiments with colloids and grains. In particular, with increasing d the distribution of particle displacements (the self-van Hove function) loses its second peak associated with hopping [16], the critical power-law regimes lengthen [41], and the SER breakdown weakens [15, 16, 40], which motivates investigating corrections to iRFOT in a controlled way.

Here we develop a way to isolate the simplest of these corrections, i.e., hopping, by studying a finite-dimensional mean-field model. Through the use of the cavity reconstruction methodology developed in the context of spin glass and information theory [42], we carefully describe caging using self-consistent equations that can be solved numerically. We can thus compute the cage width distribution and isolate hopping processes. Our results provide an unprecedentedly clear view of the impact of hopping on the dynamical transition and on the SER breakdown in simple glass formers.

MK Model - We consider the infinite-range variant of the hard sphere (HS)-based model proposed by Mari and Kurchan (MK) for simple structural glass formers [43–45] (see SI Sec. IA for details). The key feature of the MK model is that, even though each sphere has the same diameter σ, pairs of spheres interact via an additional constant shift that is randomly-selected over the full system volume. This explicit quenched disorder eliminates the possibility of a crystal state, suppresses coherent activated barrier crossing that leads to glass-glass nucleation [44], and diminishes the possibility of facilitated hopping (as we discuss below). Yet at finite densities the number of neighbors that interact with a given particle is finite and therefore finite-dimensional corrections related to hopping remain, in principle, possible.

MK liquids have a trivial structure. Even in the dense and strongly interacting regime, the pair correlation in the liquid phase is simply $g_2(r) = \theta(r-\sigma)$ (where $\theta(x)$ is the Heaviside step function), because particles are randomly displaced in space. In addition, even if both particles i and k are nearby particle j they need not be close neighbors, hence all higher-order structural correlations are perfectly factorizable. Because only two-body correlations contribute, the virial series can be truncated at the second virial coefficient [44], hence the equation of state for pressure is trivially $\beta P/\rho = 1 + B_2\rho$, where $B_2 = V_d(1)\sigma^d/2$ is the second-virial coefficient for d-dimensional hard spheres, $V_d(R)$ is the volume of a d-dimensional ball of radius R, ρ is the number density (the packing fraction $\varphi = \rho V_d(\sigma/2)$), and the inverse temperature β is set to unity [43–45] (see SI Sec. IA).

Note that these structural features hold for the liquid phase of the MK model in all d, *and* for standard HS liquids in the limit $d \to \infty$ [8, 46]. The MK model therefore coincides with standard HS in that limit. For a given finite d, however, MK liquids are structurally more similar to their $d \to \infty$ counterparts than HS liquids are. One thus sidesteps having to take into account the nontrivial structure of $g_2(r)$, which muddles the description of standard finite-dimensional HS [8].

For the MK model, one can easily construct *equilibrated* liquid configurations at all φ, even for $\varphi > \varphi_{\rm d}$ (For standard HS, by contrast, prohibitively long molecular dynamics (MD) simulations are necessary in this regime.) This dramatic speedup is accomplished by adapting the *planting* technique developed in the context of information theory [47] (see SI Sec. IB). It is thus possible to study MK liquids arbitrarily close to, both above and below, the dynamical glass transition at $\varphi_{\rm d}$. A systematic study of caging beyond $\varphi_{\rm d}$ is also possible thanks to the cavity reconstruction formalism, a method adapted from the statistical physics of random networks [42].

Caging - The MK model dynamics is studied by event-driven MD simulations of planted initial configurations with $N = 4000$ particles (see SI Sec. IB for details) [37, 38]. The mean square displacement (MSD) $\Delta(t) = \langle \sum_{i=1}^{N} [\mathbf{r}_i(t) - \mathbf{r}_i(0)]^2 \rangle / N$ is determined from time evolution of the particle positions $\mathbf{r}_i(t)$. At short times, before any collision occurs, ballistic motion gives $\Delta(t) = dt^2$; at long times, diffusive motion gives $\Delta(t) \sim 2dDt$. From $\tilde{\varphi}_{\rm onset}$ onwards, the ballistic and the diffusive regimes are separated by an intermediate caging regime where $\Delta(t) \approx \bar{\Delta}$ is approximately constant, first appearing as an inflection point and then as a full-fledged plateau (see SI Sec. IC for definition). Simply put, after a few collisions with its neighbors, a particle becomes confined to a small region of space of linear size $\sqrt{\bar{\Delta}}$, from which it can only escape, and henceforward diffuse, after a very large number of collisions.

In the $d \to \infty$ iRFOT scenario, a sharp dynamical transition occurs at $\varphi_{\rm d}$ [6, 8, 10], beyond which complete caging results in an infinitely-long plateau and in the disappearance of the diffusive regime. In finite-dimensional systems, one can use an approximate theory based on a Gaussian assumption for the cage shape, to obtain a prediction for $\varphi_{\rm d}$ and Δ [8, 45] (see SI Sec. IIA). One can also estimate $\tilde{\varphi}_{\rm d}$ from the simulation results by fitting the diffusivity using the mean-field critical form $D \sim (\varphi - \tilde{\varphi}_{\rm d})^{\tilde{\gamma}}$, and $\bar{\Delta} = \lim_{t\to\infty} \Delta(t)$ beyond $\tilde{\varphi}_{\rm d}$ (Fig. 1a). As expected from the suppression of various finite d corrections, the critical power-law regime is much longer for the MK model than for standard finite-dimensional HS (Fig. 1b) [44]. Marked qualitative discrepancies from the iRFOT predictions are nonetheless observed. (i) Numerical estimates for $\tilde{\varphi}_{\rm d}$ systematically deviate from the approximate Gaussian result for φ_d (Fig. 1c), even though the two quantities grow closer with dimension. (ii) The diffusion time $\tau_D = \sigma^2/D$ and the structural relaxation time $\tau_\alpha \propto \eta$ (see SI Sec. IC for definitions and a discussion of this point) follow the SER, $\tau_D \propto \tau_\alpha$, from $\tilde{\varphi}_{\rm onset}$ to $\varphi_{\rm SER} < \tilde{\varphi}_{\rm d}$, but then the SER breaks down, $\tau_D \propto \tau_\alpha^{1-\omega}$ with $\omega \approx 0.22$, in all d (Fig. 1d). With increasing d, however, the timescale for this crossover, $\tau_D(\varphi_{\rm SER})$, also increases (Fig. 1d), and thus $\varphi_{\rm SER}$ grows closer to $\varphi_{\rm d}$ and $\tilde{\varphi}_{\rm d}$ (Fig. 1c). (iii) Even above $\tilde{\varphi}_{\rm d}$, a steady drift of the MSD plateau can be detected (Fig. 1a), but the magnitude of this effect diminishes with increasing d.

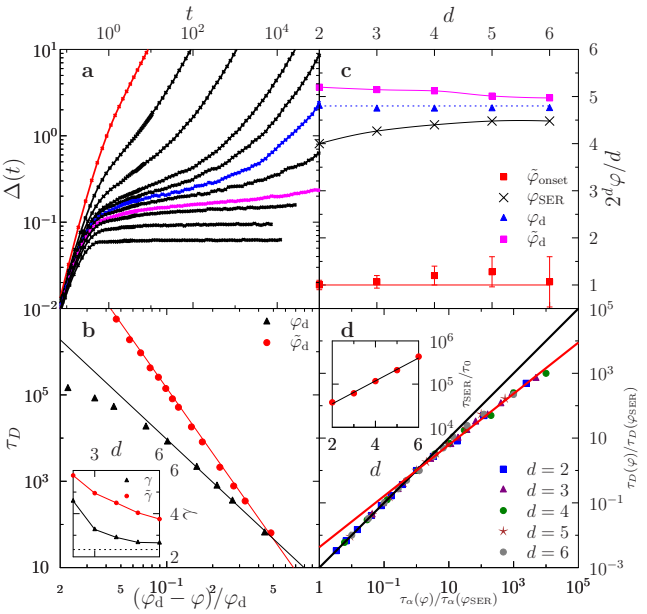

FIG. 1: (a) MSD of the MK model in $d = 3$ for φ =0.40, 1.00, 1.40, 1.65, 1.72, 1.78, 1.84, 1.93, 2.00, 2.20, and 2.50, from top to bottom. The onset of caging $\tilde{\varphi}_{\rm onset}$ (red), the theoretical dynamical transition $\varphi_{\rm d}$ (blue), and its dynamical estimate $\tilde{\varphi}_{\rm d}$ (magenta) are highlighted. Note that at $\tilde{\varphi}_{\rm d}$ and beyond a steady drift of the MSD plateau can be detected. (b) Power-law scaling in d=3 of the characteristic time τ_D determined by fitting $\tilde{\varphi}_d$=1.93 and $\tilde{\gamma}$=4.95 and by using the idealized mean-field result $\varphi_{\rm d}$=1.78 and by fitting γ=3.27. (inset) Dimensional evolution of γ and $\tilde{\gamma}$. The dashed line indicates the $d = \infty$ result γ=2.33786 [34]. Solid lines are guides for the eye. (c) The dimensional scaling of $\tilde{\varphi}_{\rm d}$, $\varphi_{\rm d}$, and $\varphi_{\rm SER}$ converges as d increases, while the onset of caging at $\tilde{\varphi}_{\rm onset}$ remains clearly distinct. The dashed line is the replica result $\varphi_{\rm d} = 4.8d2^{-d}$ [8, 10]. Solid lines are guides for the eye. (d) Dimensional rescaling of the SER (black) and SER breakdown (red) regimes for the MK model with ω=0.22. (inset) The ratio $\tau_{\rm SER}/\tau_0$ grows exponentially with d (solid line), where $\tau_{\rm SER} = \tau_D(\varphi_{\rm SER})$ and τ_0 is the microscopic time, i.e., the characteristic time for the decay of the velocity autocorrelation function [48] (see SI Sec. IC2 for details).

In order to clarify the physical origin of the above discrepancies, we first determine whether the mismatch between $\tilde{\varphi}_{\rm d}$ and $\varphi_{\rm d}$ is due to the hypothesis made in computing the latter, i.e., that all the cages have a Gaussian shape of a fixed diameter $\bar{\Delta}$, by using the cavity reconstruction formalism to relax both assumptions [42]. Above $\tilde{\varphi}_{\rm d}$, we can build the equilibrated neighborhood of particle i in order to self-consistently determine the

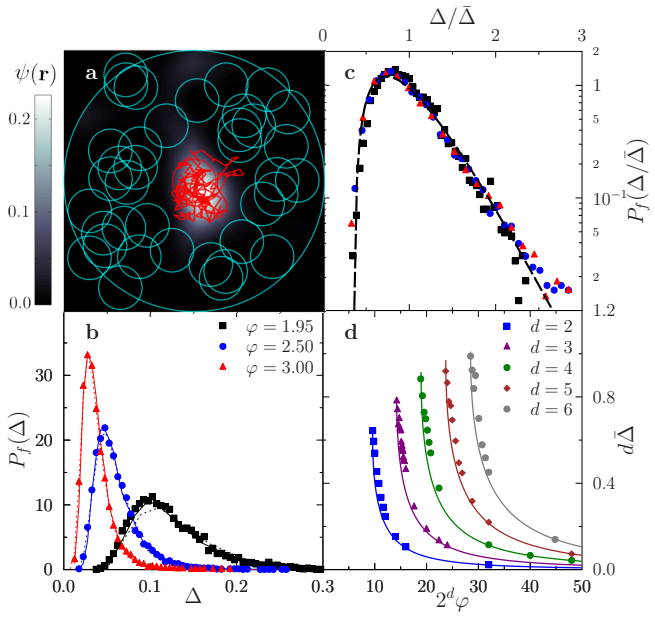

FIG. 2: (a) Illustration of a cavity reconstruction in d=2 for a perfectly caged particle at the center. Neighboring particles at their equilibrium positions (circles) provide an effective field $\psi(\mathbf{r})$ that cages the trajectory of the central particle (red line). (b) Examples of $P_f(\Delta)$ in d=3 from the cavity reconstruction formalism for Gaussian (straight lines) and ball (dashed lines) cage shapes compared with MD results (symbols). (c) Rescaled $P_f(\Delta)$ superimposed with a log normal distribution (dashed line). (d) Density evolution of $\bar{\Delta}$ measured from MD simulations (points) superimposed on the theoretical predictions of Refs. [8, 45] (lines).

overall cage size and/or shape distribution $P_f(\Delta)$ (see SI Sec. IIA for details). The process involves placing Poisson-distributed neighbors j that are randomly assigned a cage size Δ_j from a prior guess of $\tilde{P}_f(\Delta)$, with a fixed function shape $f_{A_j}(\mathbf{r})$ (a Gaussian or a ball function, for instance). Averaging over the vibrational relaxation of each neighboring particle gives the cavity field $\psi(\mathbf{r})$ felt by particle i, which is the probability density of the particle being at position $\mathbf{r}$ (Fig 2a). The existence of a cage centered around i is guaranteed by the cavity reconstruction procedure. The variance $\langle \delta\mathbf{r}^2 \rangle = \langle \mathbf{r}^2 \rangle - \langle \mathbf{r} \rangle^2$ associated with the evolution of particle i within this cage, which can be computed through simple Monte Carlo sampling, provides the posterior caging radius Δ_i. Sufficient repeats of this determination provides a new estimate of $\tilde{P}(\Delta)$, and iterating the overall procedure eventually converges to a fixed point distribution $P_f(\Delta)$. We find that both Gaussian and ball caging functions give the same size distribution $P_f(\Delta)$ (Fig 2b), and that $P_f(\Delta)$ is reasonably well approximated by a gamma distribution for all $\varphi > \varphi_\mathrm{d}$ (Fig 2c). The average cage size $\bar{\Delta}$ also quantitatively agrees with the analytical prediction of Refs. [8, 45] (Fig 2d), including its characteristic square-root singularity upon approaching φ_d, i.e., $\bar{\Delta}(\varphi_\mathrm{d}) - \bar{\Delta}(\varphi) \sim \sqrt{\varphi - \varphi_\mathrm{d}}$. Therefore, the theoretical prediction of $\bar{\Delta}$ and φ_d is fairly insensitive to the caging form and the second (or higher) moments of the cage size distribution, as well as to the method we choose (see SI Sec. IIA).

It follows that deviations from the $d \to \infty$ scenario ought to be ascribed to an imperfect caging above φ_d in finite-dimensional systems. Microscopically, these imperfections correspond to particles trapped for a finite time before escaping to another cage through a narrow passage (Fig. 3a). Because the above calculations solely consider single-cage forms, a fixed-point distribution $P_f(\Delta)$ can only be reached by removing these "hopping" segments of the particle trajectories (see SI Sec. IIA for details). Not only does $\tilde{\varphi}_\mathrm{d}$ then appears at higher densities, but as long as the network of connected cages percolates dynamical arrest is formally impossible. In that context, it is interesting to note that for a prior $\tilde{P}_f(\Delta) = \delta(\Delta)$, the first iteration of the cavity reconstruction formalism is analogous to the void (Swiss-cheese) percolation setup for a Poisson process [49]. In addition, for a non-trivial distribution of cage sizes, thresholding volume exclusion maps cavity reconstruction onto void percolation for polydisperse spheres [50] (see SI Sec. IIC). This equivalence between cavity reconstruction and void percolation sheds light on the single-cage assumption. In the iRFOT description, the MSD of each particle should remain finite when $\varphi > \varphi_\mathrm{d}$, but by construction the MSD can only be truly bounded if (minimally) $\varphi > \varphi_\mathrm{p}$, the void percolation transition.

From MD simulations of the MK model, we detect the first hopping event of each particle (see SI Sec. IIIA for details). Around φ_d, mode-coupling and hopping processes mix, but hopping quickly dominates the dynamics upon increasing φ. Although the hopping of a particle does not leave an empty void in the MK model, it can nonetheless unblock a channel for a neighboring particle to leave its cage and hence facilitate its hopping. Facilitation is thus present, but weaker than in standard finite-dimensional HS, especially at high densities. Weakened facilitation is notably signaled by the fact that the distribution of hopping times computed from a regular MD simulation largely coincides with the distribution obtained in the cavity procedure, where a single particle hops in an environment where neighboring particles are forbidden to do so (Fig. 3b inset). We find the cumulative distribution of hopping times over the accessible dynamical range to be well described by a power law $G_\mathrm{h}(t) = (t/\tau_\mathrm{h})^{1-\mu}$ (Fig. 3b), with the characteristic hopping time τ_h increasing roughly exponentially with $\varphi > \varphi_\mathrm{d}$ and markedly increasing with d (Fig. 3d). This Arrhenius-like scaling form is consistent with a gradual and uncorrelated narrowing of the hopping channels with φ. Note that similar phenomenological power-law distributions have recently been reported for other glass-forming systems, such as the bead-spring model for polymer chains [51]. We get back to this point in the conclusion.

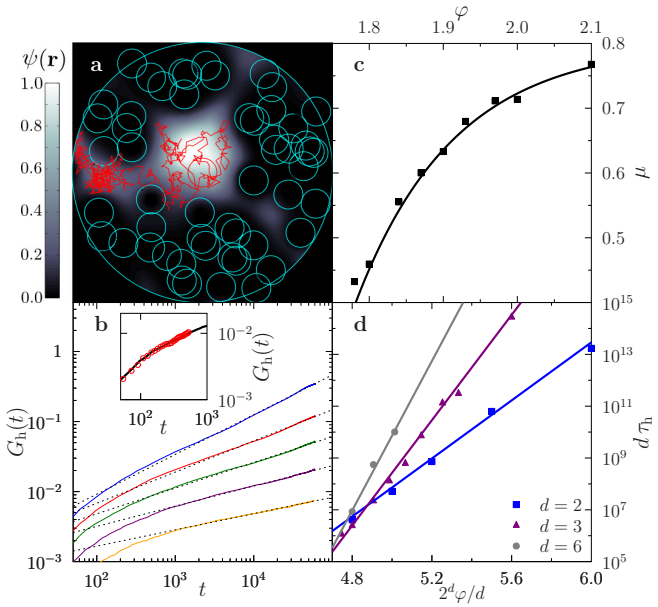

FIG. 3: (a) Illustration of a cavity reconstruction in $d = 2$ for a hopping particle. In this case the neighboring particles allow the central particle to hop to other cages (red line). (b) Cumulative time probability distribution of hopping events $G_h(t)$ for $d = 3$ systems at densities (from top to bottom) $\varphi = 1.78, 1.84, 1.90, 1.97$, and 2.10, along with the power-law scaling form (dashed line). (inset) Single-particle hopping from the cavity reconstruction (circles) overlays with the MD simulations at short times ($\varphi = 1.90$). Phenomenological scaling parameters (c) μ and (d) τ_h for the probability distribution of hopping events. Solid lines are a guide for the eye for μ and exponential fits for τ_h.

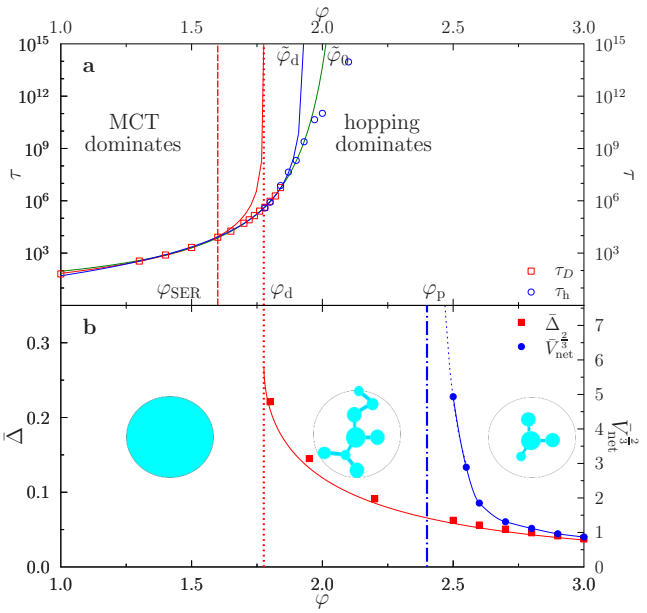

FIG. 4: (a) Dynamical and (b) static phase diagrams for the MK model in $d = 3$. Early in the critical regime, the relaxation times scale like a power-law, but beyond φ_{SER} hopping causes large deviations from this scaling. An effective $\tilde{\varphi}_d$ is numerically detected instead. A VTF scaling fits the data even better. Statically, cages can be detected from φ_d onwards by removing hopping. In reality, the fine inter-cage channels that allow hopping, however, result in a cage network. Beyond φ_p the typical network stops percolating and the network volume scales critically $\bar{V}_{net} \sim (\varphi - \varphi_p)^{-1.8}$ with $\varphi_p = 2.40$ (dashed blue line) [49, 52]. The single-cage limit is reached when $\bar{V}_{net} \sim \bar{\Delta}^{3/2}$.

Finite-dimensional phase diagram - A clear scenario for hopping in the MK model follows (Fig. 4). Dynamically, the system becomes increasingly sluggish upon increasing φ above $\tilde{\varphi}_{onset}$. Initially, cages are not well formed and the slowdown exhibits a power-law scaling, according to the iRFOT critical predictions. Hopping cannot be defined because cages are too loose. Upon approaching φ_d, however, cages become much longer-lived. In this regime, iRFOT predictions give a rapidly growing τ_D, but hopping processes allow particles to escape their cages and diffuse, hence providing a cutoff to the critical divergence of τ_D. The critical-like behavior of the diffusivity is also pushed to denser systems, and fitting to a power-law gives $\tilde{\varphi}_d > \varphi_d$. When τ_D is comparable to τ_h a mixed regime emerges, characterized by a SER breakdown, as we discuss below. Even beyond $\tilde{\varphi}_d$, however, the dynamics is not fully arrested. Hopping remains possible, which shows that $\tilde{\varphi}_d$ has no fundamental meaning and is just a fitting parameter associated to an effective power-law divergence of τ_D. In fact, the MK dynamical data are better fitted by a VTF form than by the critical power-law (Fig. 4a), although the fitting parameter φ_0 has no direct static interpretation because it is intermediate between φ_d and φ_p.

The dynamics can also be understood from the organization of cages. The critical density φ_d of iRFOT corresponds to the emergence of a connected network of cages. Typical networks for $\varphi_d < \varphi < \varphi_p$ span the system volume. When $\varphi > \varphi_p$, they become finite and the mean network volume $\bar{V}_{net}$ (sum of cage volumes in the network) follows a critical scaling from standard percolation (Fig. 4b). Based on this analysis, in the absence of facilitation the dynamical arrest should take place at φ_p [53]. Note that although above φ_p the single-particle MSD is bounded, a particle can still explore a finite number of cages. Perfect single-cage trapping can only be found at $\varphi \to \infty$ in finite d. Hopping is then infinitely suppressed because both the width and the number of hopping channels between cages vanish. However, even if hopping interferes with caging, well above φ_d vibrational relaxation within the cage is sufficiently quick to numerically distinguish it from hopping. This large separation of timescales enables the facile detection of hopping in MD simulations and cavity reconstruction. But upon approaching φ_d the task becomes acutely sensitive to the arbitrary thresholding inherent to any hopping detection algorithm [22, 54] (see SI Sec. IIIA for details).

As expected from the exactness of the iRFOT descrip-

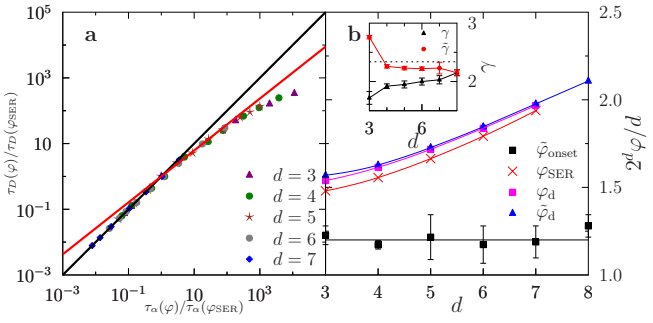

FIG. 5: (a) Dimensional rescaling of the SER (black) and SER breakdown regimes for standard finite-dimensional HS. The early deviation exponent ω is consistent with hopping in the MK model with $\omega = 0.22$ (red line, see Fig. 1d), but a growing deviation is observed as φ increases. (b) The dimensional scaling of HS results for $\tilde{\varphi}_{\rm d}$, $\varphi_{\rm d}$, and $\varphi_{\rm SER}$ converge as d increases, while $\tilde{\varphi}_{\rm onset}$ remains distinctly smaller (compare with Fig. 1c). Note that in $d = 8$, $\tilde{\varphi}_{\rm d}$, $\varphi_{\rm d}$, and $\varphi_{\rm SER}$ are numerically indistinguishable. (inset) Dimensional evolution of γ and $\tilde{\gamma}$. Both of which are consistent with the $d = \infty$ result (dashed line). Solid lines are guides for the eye.

tion in $d \to \infty$, $\tilde{\varphi}_{\rm d}/\varphi_{\rm d} \to 1$ with increasing d. Both $\tilde{\gamma}$ and γ also appear to converge to the $d = \infty$ value (Fig. 1b) [34]. Because $\varphi_{\rm d} < \varphi_{\rm p}$ for all d, the suppression of hopping with increasing d (see Fig. 1d inset) ought to be ascribed either to the narrowing of the hopping channels or to topological changes to the cage network. Because the pressure at the dynamical transition increases only slowly with dimension ($p_{\rm d} \sim d$), the typical channel width is expected to stay roughly constant. The topology of the cage network, however, has a larger dimensional dependence. The cage network at percolation, for instance, has a fractal dimension $d_{\rm f} \ll d$ [52], e.g, $d_{\rm f} = 4$ for $d \geq d_u = 6$. Although this result is only valid at $\varphi_{\rm p}$ proper, the *local* network structure persists at smaller φ because the loss of the cage network fractality takes place through the single-point inclusion of non-percolating clusters [52]. The network topology is therefore such that the hopping channels (even assuming that their cross-section remains constant) cover a vanishingly small fraction of the cage surface as d increases. The limited number of ways out of a local cage thus entropically suppresses hopping.

SER Breakdown - With hopping events clearly identified, it becomes possible to isolate the pure critical iRFOT (or mode-coupling) regime. Within this regime, we obtain a power-law scaling that is consistent with $\varphi_{\rm d}$ (see SI Sec. IIB for details), and the SER is followed. Deviations from the extrapolated critical scaling coincide with the SER breakdown in all d. Although $\tilde{\varphi}_{\rm onset}$ occurs at a roughly constant distance from $\varphi_{\rm d}$, the SER breakdown occurs in systems that are increasingly sluggish with d, $\varphi_{\rm SER} \to \varphi_{\rm d}$, and thus properly converges to the idealized mean-field behavior as $d \to \infty$. In the MK model, the SER breakdown is thus clearly due to hopping.

By modifying the cavity reconstruction analysis, a self-consistent caging determination of $\varphi_{\rm d}$ and $\varphi_{\rm p}$ should also be possible for standard finite-dimensional HS. We do not attempt such a computation here, but instead use the insights gained from the MK model to associate the SER breakdown in HS with hopping. We fit the dynamical data from the regime over which the SER is obeyed to extract $\varphi_{\rm d}$ and γ, and the full dynamical regime to extract $\tilde{\varphi}_{\rm d}$ and $\tilde{\gamma}$ [38]. As for the MK model, the two procedures converge as d increases (Fig. 5), while $\tilde{\varphi}_{\rm onset}$ clearly remains distant, as is observed in many other glass formers [55, 56]. Interestingly, for HS, $\varphi_{\rm SER}$ and $\varphi_{\rm d}$ are relatively close to begin with. The fairly structured pair correlation function in HS and the much larger pressure at $\varphi_{\rm d}$ lead to smaller interparticle gaps. Particles are thus caged more efficiently, which suppresses hopping.

Contrasting Figs. 1d and 5a suggests that near $\varphi_{\rm SER}$ the SER breakdown exponent ω is similar for HS and the MK model. In this regime, HS hopping is consistent with MK-like hopping. In HS, however, single-particle hopping leaves an actual structural void that enhances the correlation (and hence the facilitation) of hopping events [27–29]. As HS become more sluggish, cooperativity plays a growing role. As a result, a pronounced difference between HS and MK hopping for $\varphi \gg \varphi_{\rm SER}$ can be observed. The lack of a notable dimensional dependence of the master curve suggests that if the SER breakdown is also affected by critical fluctuations, as suggested in Ref. [17], that effect may be hard to detect. In contrast to Ref. [16], we now understand the reduction of the measured ω as d increases to a delayed onset of hopping.

Conclusions - We have numerically and theoretically studied a model glass former in which it is possible to isolate hopping from the critical mode-coupling dynamical slowing down, and in which no other dynamical effects are present besides these two. The results illuminate the key role played by hopping in suppressing the iRFOT dynamical transition in finite-d and in breaking the SER scaling. The MK model gives an example where single-particle hopping is sufficient to cause the SER breakdown, but in HS facilitation likely amplifies the effect, which could explain the dependence of ω on density (Fig. 5) [57].

For standard finite-dimensional HS and other structural glass formers, we expect the situation to be made more complex by the other dynamical processes mentioned in the introduction. One might then conjecture the existence of at least three dynamical regimes for glass formers, upon increasing density. (i) A iRFOT/mode-coupling regime below $\varphi_{\rm SER}$. (ii) A MK-like hopping regime around $\varphi_{\rm SER}$, where hopping is the dominant correction to the iRFOT description, the mode-coupling critical scaling holds but the apparent mode-coupling transition shifts to higher densities and the effective exponent γ changes, and the SER breakdown is incipient. In this regime the hopping timescale increases (exponentially) quickly with density (Fig. 3d). We expect this increase to be similar for HS and MK liquids, because

the probability of finding a neighboring cage is roughly $\exp(-\varphi)$ for both models. (iii) At yet higher densities, hopping becomes too slow and other dynamical effects likely become important. If glass-glass nucleation barriers do not grow as quickly as the hopping barriers, then these processes may eventually become the dominant relaxation mechanism, following the RFOT prediction [5, 12, 31]. In this regime (hence in deeply supercooled liquids much below $T_{\rm d}$) the VTF law and the associated Adam-Gibbs relation should be reasonably well obeyed. Note that other processes such as cooperative hopping dressed by elasticity might also occur in this regime [26]. Note also that these different regimes are probably not separated by sharp boundaries in realistic systems, hence all these relaxation processes might coexist, making their identification quite challenging.

We would also like to stress, in line with previous studies, that VTF fits of the structural relaxation time in regimes (i) and (ii) should not be used to extract the putative Kauzmann transition point. In our opinion it makes no sense to test the Adam-Gibbs relation in these dynamical regimes. In the MK model, although the VTF law can be used to fit the dynamical data, there is indeed no associated Adam-Gibbs relation and φ_0 has no thermodynamic meaning. In particular, φ_0 is *not* associated with a Kauzmann transition (which in the MK model only happens at $\varphi = \infty$ [44]). This observation is particularly important for numerical simulations and experiments on colloids and granular systems, which are most often performed in the vicinity of $\varphi_{\rm d}$ and $\varphi_{\rm SER}$, and hence are found within the first two regimes.

Finally, we note that the MK model could also serve as a test bench for descriptions of hopping [24, 25, 58], as well as for relating percolation and glassy physics more broadly [59]. These studies may clarify other finite-dimensional effects, such as the correlation observed between local structure and dynamics [30].

Acknowledgments We thank G. Biroli, J.-P. Bouchaud, D. Chandler, J.-P. Garrahan, J. Kurchan, D. Reichman, C. Rycroft, and G. Tarjus for stimulating discussions. Financial support was pro- vided by the European Research Council through ERC grant agreement no. 247328 and ERC grant NPRGGLASS. P.C. acknowledges support from the Alfred P. Sloan Foundation.

Supplementary Information

Contents

A. Introduction 8
1. The model 8
2. Simulation details 10
a. Molecular dynamics simulations 10
b. Planting 10
3. Basic phenomenology of glassy behavior and definitions of physical quantities 11
a. Mean square displacement (MSD) and cage sizes 11
b. Characteristic timescales 12
c. Characteristic densities 13

B. Caging 15
1. Thermodynamics: the caging order parameter and the dynamic transition density 15
a. Calculation of the mean caging order parameter: the replica method 15
b. Calculation of the cage size distribution: the cavity method 16
c. Comparing theoretical predictions with simulations 19
2. Caging dynamics: mode-coupling theory (MCT) and beyond 20
a. Testing the mode-coupling theory 20
b. Breakdown of the Stokes-Einstein relation 21
3. Percolation of the cage network 22
a. Mapping the glass transition to a void percolation transition 22
b. Methodology for determining the void percolation threshold 23

C. Hopping 25
1. Detecting hopping 25
2. Hopping dynamics 26

References 26

Appendix A: Introduction

1. The model

The infinite-range variant of the Mari-Kurchan (MK) model [44] is defined by adding to the distances between pairs of particles an additional quenched random shift that spans the whole system size (Fig. 6a). The Hamiltonian for N hard spheres (HS) is thus

$$\mathcal{H} = \sum_{i<j}^{N} U(|\mathbf{r}_i - \mathbf{r}_j + \mathbf{\Lambda}_{ij}|), \tag{A1}$$

where $U(r)$ for $|\mathbf{r}| = r$ is the HS potential ($e^{-\beta U(r)} = \theta(r-\sigma)$), for spheres of diameter σ, and $\mathbf{\Lambda}_{ij}$ is a uniformly distributed vector within the system volume V, i.e., with a probability distribution $P(\mathbf{\Lambda}_{ij}) = 1/V$. Note that the standard HS model corresponds to $\mathbf{\Lambda}_{ij} = 0$.

Note that even if in principle all particles interact with all others, in practice because $U(r)$ is short-ranged, a given particle only interacts directly with a finite number of neighbors (the first coordination shell), as in usual liquids. Hence, the model is akin to a mean-field spin-glass model with finite connectivity with the connectivity depending on the number of neighbors in the first coordination shell, and thus on both density and dimension.

MK liquids have a simple structure in all spatial dimension d, because random shifts eliminate higher-order correlations. For example, consider two particles j and k both near particle i, i.e., $|\mathbf{r}_i - \mathbf{r}_j + \mathbf{\Lambda}_{ij}| \approx \sigma$ and $|\mathbf{r}_i - \mathbf{r}_k + \mathbf{\Lambda}_{ik}| \approx \sigma$. Unlike in regular HS, in the MK model particles j and k have a negligible probability of being near each other ($|\mathbf{r}_j - \mathbf{r}_k + \mathbf{\Lambda}_{jk}| > \sigma$), because their effective distance is shifted by $\mathbf{\Lambda}_{jk}$, which is of the order of the system size. This argument can also be generalized to interactions between more particles. Particle i thus has hard-core interactions

with its neighbors, but with probability one in the thermodynamic limit these neighbors can overlap with each other. The two-point correlation function seen from one particle is simply

$$g_2(\mathbf{r}) = \overline{\left\langle \frac{1}{N}\sum_{i\neq j}\delta(\mathbf{r}_{ij}-\mathbf{r})\right\rangle}^{\mathbf{\Lambda}} = \theta(|\mathbf{r}|-\sigma)\ , \tag{A2}$$

where $\mathbf{r}_{ij} = \mathbf{r}_i - \mathbf{r}_j + \mathbf{\Lambda}_{ij}$.

Let $V_{\rm d}(\sigma/2)$ be the volume of a d-dimensional ball of diameter σ, and $V_{\rm d} = V_{\rm d}(1)$. For the MK model, the virial expansion of the equation of state (EOS) terminates at the second-order

$$\begin{aligned} p &= 1 + B_2\rho = 1 + 2^{d-1}\varphi\ , \\ S_{\rm liq}^{\rm MK} &= 1 - \log\rho\lambda^d - 2^{d-1}\varphi + \ln N, \end{aligned} \tag{A3}$$

where $p = \beta P/\rho$ is the reduced pressure with β the inverse temperature and $\rho = N/V$ the number density, $\varphi = \rho V_d(\sigma/2) = \rho V_d 2^{-d}$ is the packing fraction (we set $\sigma = 1$), $S_{\rm liq}^{\rm MK}$ is the liquid entropy per particle, λ is the thermal de Broglie wavelength, and $B_2 = V_d/2$ is the HS second virial coefficient.

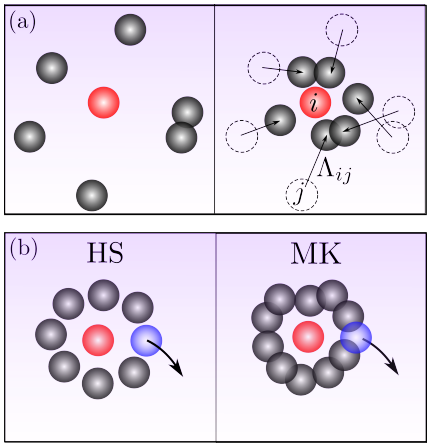

FIG. 6: (a) Illustration of the MK model. Left: particles in the original space. Right: particles in the shifted space with respect to particle i (red). Although neighbors cannot overlap with particle i, they are allowed to overlap with each other because of the random shifts. (b) Comparing hopping in the HS and the MK models. Left: in HS, removal (hopping) of a neighbor (blue) creates an open channel for the caged particle (red) to hop. Right: In MK, removing a neighbor is much less likely to open a channel because the other neighbors are allowed to overlap.

Compared to HS, the MK model has several unique features. (i) Although monodisperse HS easily crystallize in low dimensions, the random shifts in the MK model impose a quenched disorder that is incompatible with crystal symmetry and fully suppresses the crystal phase. (ii) Glass-glass nucleation [5, 31] is also suppressed, because if a nucleus forms around a particle, the particles inside this nucleus are actually randomly distributed in real space and thus no surface can be formed (Fig. 6). The free energy cost of forming a nucleus hence scales with the system size and diverges in the thermodynamic limit. (iii) Particle hopping is much less correlated. By contrast to HS, where the hopping of a particle increases the chance that one of its neighbors also hops due to the real-space void it leaves behind, facilitation is limited to unblocking an escape channel in the MK model (Fig. 6b). (iv) MK particles are distinguishable because the quenched shifts $\{\mathbf{\Lambda}_{ij}\}$ are fixed. Besides the lack of structure, the partition function Z of the MK model is therefore different from that of HS by a factor of $N!$, i.e., $Z_{\rm MK}/N! \sim Z_{\rm HS}$, and hence $S_{\rm liq}^{\rm MK} \sim S_{\rm liq}^{\rm HS} + \ln N$. As a result, the density of the Kauzmann transition in MK diverges in the thermodynamic limit [44].

Introducing a set of quenched random shifts brings two key advantages from a methodological point of view. First, in computer simulations, it is convenient to "plant" an equilibrated MK configuration (Sec. A 2 b). Planting avoids the (circular) difficulty encountered in most other glass-forming liquids of equilibrating an initial liquid configuration before studying its equilibrium relaxation dynamics. Second, one can map the model onto a constraint satisfaction problem defined on a random graph (Bethe lattice). It is therefore possible to study its properties with the cavity method (Sec. B 1 b), which is, in principle, exactly solvable.

2. Simulation details

a. Molecular dynamics simulations

We adapt the event-driven molecular dynamics (MD) algorithm of Refs. [37, 38, 41] for HS to simulate the MK model in dimensions $d = 2 - 6$ with $N = 4000$ particles. Periodic boundary conditions with the minimum image convention are implemented on the shifted distances $|\mathbf{r}_i - \mathbf{r}_j + \mathbf{\Lambda}_{ij}|$. For each φ, we perform 8 independent realizations, each corresponding to a different set $\{\mathbf{\Lambda}_{ij}\}$ for a planted initial configuration (see Sec. A 2 b). Simulations are run at constant unit β, for a time t (given in units of $\sqrt{\beta m \sigma^2}$, where the particle mass m is also set to unity) sufficiently long to reach either the diffusive regime in the liquid or the asymptotic plateau in the glass. As described in Refs. [16, 41], HS data is obtained from simulations of $N = 8000$ identical particles in $d = 4 - 8$, and, in order to prevent the system from crystallizing [60], from a HS binary mixture with diameter ratio $\sigma_2/\sigma_1 = 1.2$ in $d = 3$ [16] .

b. Planting

Planting, which here consists of switching the order of determining initial particle positions $\{\mathbf{r}_i\}$ and constraints $\{\mathbf{\Lambda}_{ij}\}$, is an expedient technique for studying equilibrium ensembles in random constraint satisfaction problems [47]. In general, the planted ensemble is different from the annealed ensemble, but for the liquid phase it can be shown that both are equivalent, as we detail below.

In the following, we will be interested in physical observables $\mathcal{F}$ that depend on some initial condition $\{\mathbf{r}_i\}$ and on their time evolution under deterministic MD dynamics, e.g. the mean square displacement defined in Eq. (A7). In the presence of disorder, the average of physical observables should be measured by the so-called "quenched" average

$$\overline{\langle \mathcal{F} \rangle^{\mathbf{\Lambda}}} \equiv \int \prod_{i<j}^{N} d\mathbf{\Lambda}_{ij} P(\mathbf{\Lambda}_{ij}) \left(\frac{\int \prod_{i=1}^{N} d\mathbf{r}_i \mathcal{F} e^{-\beta \mathcal{H}}}{\int \prod_{i=1}^{N} d\mathbf{r}_i e^{-\beta \mathcal{H}}} \right), \tag{A4}$$

where $\mathcal{F}$ and $\mathcal{H}$ depend on both $\{\mathbf{r}_i\}$ and $\{\mathbf{\Lambda}_{ij}\}$. In fact, because the disorder is independent of time for a given sample, one should first perform the thermal ensemble average $\langle \mathcal{F} \rangle$ for a given realization of disorder, and then repeat this operation for many extractions of $\{\mathbf{\Lambda}_{ij}\}$ to average over the disorder. In simulations, however, once $\{\mathbf{\Lambda}_{ij}\}$ is fixed, equilibrating independent configurations at large φ is very time consuming, because one should first anneal the system quasi-statically slowly up to the desired density.

Let us define the so-called "annealed" average:

$$\langle \mathcal{F} \rangle_{\mathrm{a}} \equiv \frac{\int \prod_{i<j}^{N} d\mathbf{\Lambda}_{ij} P(\mathbf{\Lambda}_{ij}) \int \prod_{i=1}^{N} d\mathbf{r}_i \mathcal{F} e^{-\beta \mathcal{H}}}{\int \prod_{i<j}^{N} d\mathbf{\Lambda}_{ij} P(\mathbf{\Lambda}_{ij}) \int \prod_{i=1}^{N} d\mathbf{r}_i e^{-\beta \mathcal{H}}} = \frac{\int \prod_{i=1}^{N} d\mathbf{r}_i \int \prod_{i<j}^{N} d\mathbf{\Lambda}_{ij} P(\mathbf{\Lambda}_{ij}) e^{-\beta \mathcal{H}} \mathcal{F}}{\int \prod_{i=1}^{N} d\mathbf{r}_i \int \prod_{i<j}^{N} d\mathbf{\Lambda}_{ij} P(\mathbf{\Lambda}_{ij}) e^{-\beta \mathcal{H}}} \ . \tag{A5}$$

This average corresponds to a very different situation, where the averages over $\{\mathbf{r}_i\}$ and $\{\mathbf{\Lambda}_{ij}\}$ are interchangeable. Physically, this describes a situation where both variables and disorder fluctuate together; their timescales are indistinguishable. Mathematically, the last equality in Eq. (A5) shows that the integration measure can be obtained by first extracting a uniformly random configuration $\{\mathbf{r}_i\}$, and next extracing a configuration $\{\mathbf{\Lambda}_{ij}\}$ from the distribution

$$P(\{\mathbf{\Lambda}_{ij}\}|\{\mathbf{r}_i\}) = \left[\prod_{i<j}^{N} P(\mathbf{\Lambda}_{ij}) \right] \ e^{-\beta \mathcal{H}} = \prod_{i<j}^{N} \left[P(\mathbf{\Lambda}_{ij}) e^{-\beta U(|\mathbf{r}_i - \mathbf{r}_j + \mathbf{\Lambda}_{ij}|)} \right] \ . \tag{A6}$$

Because $P(\{\mathbf{\Lambda}_{ij}\}|\{\mathbf{r}_i\})$ is factorized, each $\mathbf{\Lambda}_{ij}$ must be extracted independently, uniformly in the volume V with the constraint that $|\mathbf{r}_i - \mathbf{r}_j + \mathbf{\Lambda}_{ij}| > \sigma$. In summary, we use the following procedure to compute $\langle \mathcal{F} \rangle_{\mathrm{a}}$:

Procedure-Planting-MK

1. Generate N particle positions $\{\mathbf{r}_i\}$ according to a Poisson (ideal gas) process.
2. For each pair of particles i and j, randomly and independently draw a vector $\mathbf{\Lambda}_{ij}$, uniformly in the sub-region of the whole volume V that is compatible with $\mathbf{r}_i$ and $\mathbf{r}_j$, $|\mathbf{r}_i - \mathbf{r}_j + \Lambda_{ij}| > \sigma$.
3. Starting from the state given by $\{\mathbf{r}_i\}$, and for the given $\{\mathbf{\Lambda}_{ij}\}$, compute the time evolution $\{\mathbf{r}_i(t)\}$ from MD simulations. From this trajectory compute $\mathcal{F}$.

4. Repeat (1-3) to average over disorder and initial configurations.

The key to the success of this approach is determining if, and under what conditions, the quenched and the annealed averages over the disorder are the same, $\overline{\langle\mathcal{F}\rangle^{\mathbf{\Lambda}}} = \langle\mathcal{F}\rangle_{\rm a}$. Equations (A4) and (A5) coincide if the equality $\overline{\log Z^{\Lambda}} = \log \overline{Z^{\Lambda}}$ holds, where $Z = \int \prod_{i=1}^{N} d\mathbf{r}_i e^{-\beta\mathcal{H}}$ is the partition function for given $\{\mathbf{\Lambda}_{ij}\}$ [47, 61, 62]. This situation arises if the fluctuations of Z induced by the fluctuations of quenched disorder $\{\mathbf{\Lambda}_{ij}\}$ are very weak in the thermodynamic limit. This condition is satisfied in the liquid phase, but is violated in the glass phase away from the equilibrium liquid line [47, 61, 62].

According to the analysis of Ref. [47], in order to check numerically that the annealed and the quenched average coincide, one should compute the vibrational (internal) entropy of the planted glass state. This can be done for example using the procedure described in Ref. [63]. If the internal entropy of the glass turns out to be larger than the liquid entropy given by Eq. (A3), then the annealing average does not coincide with the quenched average [47]. Fortunately, in the MK model the liquid entropy per particle diverges proportionally to $\log N$ (see Eq. (A3)), while the glass entropy per particle is finite, because particles cannot exchange (at least if one neglects hopping, as discussed below). Therefore, for $N \to \infty$ the liquid entropy is always larger than the glass entropy, and the annealed average is correct. In other words, because the Kauzmann transition for the MK model is located at infinite density [44], the procedure is valid.

Numerical simulations show that the annealed average done using the planting procedure discussed above is in perfect agreement with the liquid EOS Eq. (A3) (Fig. 7). This result is not a surprise, because it can easily be shown that the annealed equation leads to the same liquid EOS in Eq. (A3), but it is a consistency test for the numerical procedure. Note that the pressure remains stable over time, as it should be if one initializes the MD simulation in an equilibrium configuration.

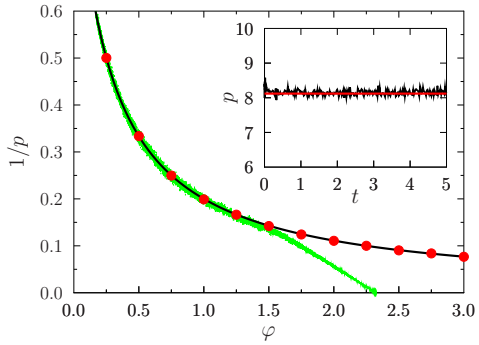

FIG. 7: Comparison between the reduced pressure p of planted states (red circles) and the liquid EOS Eq. (A3) (black solid line) in $d = 3$. The regime above $\varphi_{\rm d} = 1.776$ is numerically inaccessible from conventional slow quenching procedures (see, for example, the green line obtained from the Lubachevsky-Stillinger algorithm with a growth rate $\dot{\gamma} = 3 \times 10^{-5}$ [38]), because the system starts to deviate from the liquid EOS around $\varphi_{\rm d}$. (inset) Planting at $\varphi = 1.78$ gives the correct equilibrium pressure (red line) from $t = 0$.

3. Basic phenomenology of glassy behavior and definitions of physical quantities

Before turning to a more detailed explanation of our results, in this section we summarize the main physical observables that we investigate in this study, with a short account of their definition and of the main results.

a. Mean square displacement (MSD) and cage sizes

Despite its trivial liquid phase, the MK model presents a complex glass-forming and glassy behavior. Above the onset $\tilde{\varphi}_{\rm onset}$ of sluggish dynamics (see Sec. A 3 c for definition), We can distinguish three main regimes in the mean

square displacement:

$$\Delta(t) = \frac{1}{N}\sum_{i=1}^{N}\left\langle|\mathbf{r}_i(t)-\mathbf{r}_i(0)|^2\right\rangle \tag{A7}$$

(i) a ballistic regime with $\Delta(t) = dt^2$; (ii) a caging regime with a plateau $\Delta(t) \sim \bar{\Delta}$, where $\bar{\Delta}$ is the mean cage size; and (iii) a diffusive regime with $\Delta(t) = 2dDt$, where D is the diffusivity. According to mode-coupling theory (MCT), the plateau becomes asymptotically stable beyond the dynamical transition φ_{d} (see Sec. B 2 a). We can then formally define the mean cage size as the infinite time limit of the MSD

$$\bar{\Delta} \equiv \lim_{t\to\infty}\Delta(t), \tag{A8}$$

and the individual cage size Δ_i of each particle i

$$\Delta_i \equiv \lim_{t\to\infty}\langle|\mathbf{r}_i(t)-\mathbf{r}_i(0)|^2\rangle. \tag{A9}$$

From this definition and the equilibrium conditions $\langle\mathbf{r}_i(0)\rangle = \langle\mathbf{r}_i(t)\rangle$ and $\left\langle|\mathbf{r}_i(0)|^2\right\rangle = \left\langle|\mathbf{r}_i(t)|^2\right\rangle$, we obtain another expression for Δ_i

$$\begin{aligned}\Delta_i &= \lim_{t\to\infty}[\langle|\mathbf{r}_i(t)|^2\rangle - 2\langle\mathbf{r}_i(t)\cdot\mathbf{r}_i(0)\rangle + \langle|\mathbf{r}_i(0)|^2\rangle]\\ &= 2\lim_{t\to\infty}[\langle|\mathbf{r}_i(t)|^2\rangle - |\langle\mathbf{r}_i(t)\rangle|^2].\end{aligned} \tag{A10}$$

The definition of Δ_i in Eq. (A9) can be directly used to measure individual cage sizes in numerical simulations. Equation (A10) also suggests that Δ_i is twice the variance of the distribution of particle positions within a cage. In theoretical calculations, a cage form ansatz $f_A(\mathbf{r})$ is usually used for this distribution. Two commonly used functions are the Gaussian

$$f_A^{\mathrm{G}}(\mathbf{r}) = \frac{e^{-\frac{\mathbf{r}^2}{2A}}}{(2\pi A)^{d/2}} \tag{A11}$$

and the ball functions

$$f_A^{\mathrm{b}}(\mathbf{r}) = \frac{\theta(A-\mathbf{r}^2)}{V_d(\sqrt{A})}. \tag{A12}$$

Below, we use the Gaussian anzatz in the replica method (Sec. B 1 b), and both ansatz in the cavity method (Sec. B 1 b). The parameter A in these functions can be related to Δ_i using Eq. (A10)

$$\Delta_i = 2dA_i \tag{A13}$$

for the Gaussian function and

$$\Delta_i = \frac{2d}{d+2}A_i \tag{A14}$$

for the ball function.

b. Characteristic timescales

In this subsection, we define the characteristic timescales, their physical interpretations, and how they are numerically determined.

- τ_0 – microscopic time. This natural timescale serves as reference to compare the evolution of other timescales with spatial dimension d. Its definition is such that the velocity autocorrelation function $d(\tau_0) = 1/e$, where $d(t) = \frac{1}{dN}\sum_{i=1}^{N}\langle\mathbf{v}_i(t)\cdot\mathbf{v}_i(0)\rangle = \frac{1}{2d}\frac{d^2\Delta(t)}{dt^2}$ (see Fig. 8c) [48].
- τ_D – diffusion time. The characteristic time for diffusion time is defined as $\tau_D = \sigma^2/D$, such that $\Delta(t)$ vs t/τ_D collapses in the caging and diffusive regimes (Fig. 8a), as predicted by MCT (see Eq. (B16)). Using this collapse, we can determine τ_D without explicitly extracting D, which allows us to estimate τ_D close to the dynamical transition, even when the fully diffusive regime itself is beyond numerical reach.

- $\tau_{\rm SER}$ – characteristic time at $\varphi_{\rm SER}$, i.e., $\tau_{\rm SER} = \tau_D(\varphi_{\rm SER})$.
- τ_α – structural relaxation time. In standard glass-forming liquids, τ_α is typically extracted from the decay of the self-intermediate scattering function

$$F_s(k,t) = \frac{1}{N}\left\langle \sum_{i=1}^{N} e^{i\mathbf{k}\cdot[\mathbf{r}_i(t)-\mathbf{r}_i(0)]} \right\rangle, \tag{A15}$$

such that

$$F_s(k^*,\tau_\alpha) = 1/e, \tag{A16}$$

where k^* is the first particle peak of the structure factor

$$S(k) = 1 + \rho \int d\mathbf{r} e^{-i\mathbf{k}\cdot\mathbf{r}} g_2(\mathbf{r}). \tag{A17}$$

For the MK model, however, this method cannot be directly applied because the trivial structure of $g_2(r)$ (and hence of $S(k)$) leaves k^* ill defined. Here, we use a slightly different, although consistent, approach to measuring τ_α. We first generalize the definition of the MSD to the typical displacement of particles

$$r_{\rm typ}(t) = \lim_{z\to 0} \frac{1}{N}\sum_{i=1}^{N} \langle |\mathbf{r}_i(t) - \mathbf{r}_i(0)|^z \rangle^{\frac{1}{z}}, \tag{A18}$$

which is the zeroth moment of the self van Hove function $G_s(r,t)$, i.e., the displacement of the majority of particles at time t. In practice, to determine $r_{\rm typ}(t)$, we use $z = 0.1$ which is very close to the limit $z \to 0$. By analogy to τ_D, we then determine the relaxation time τ_α by ensuring that $r^2_{\rm typ}(t)$ vs t/τ_α collapses in the MSD caging regime (Fig. 8b). Note that τ_α is then only defined up to an overall constant that is independent of density.

For HS, this (re)definition of τ_α is consistent with the traditional one, because the condition in Eq. (A16) is equivalent to $kr_{\rm typ}(\tau_\alpha) \sim 1$. The length scale $1/k^*$ indeed corresponds to that of the maximum density fluctuation, which should be of the order of the typical cage diameter. The scaling $r_{\rm typ}(\tau_\alpha) \sim 1/k^* \sim \sqrt{\bar{A}}$ shows that $r_{\rm typ}$ is near the caging regime at τ_α, and hence should be independent of density. Our estimate of τ_α is therefore consistent with the proportionality relation for the viscosity $\tau_\alpha \sim \eta$ observed in very sluggish fluids [16]. Note that the above definitions of τ_α and τ_D give additional weight to slower and faster particles, respectively. In this context, the breakdown of SER is consistent with a proportion of fast particles that is larger than expected [14].

- $\tau_{\rm h}$ – hopping time. The typical time for a caged particle to escape (see Sec. C for more details).

c. *Characteristic densities*

In this subsection, we define the characteristic densities (number density and volume fraction are used interchangeably), their physical interpretations, and how they are numerically and theoretically determined. Results for HS and the MK model are reported in Table I.

- $\tilde{\varphi}_{\rm onset}$ – onset density of the glassy behavior. It corresponds to the lower limit of the caging regime [64]. Its choice is such that for $\varphi < \tilde{\varphi}_{\rm onset}$ no inflection point appears in the logarithmic-scale MSD; for $\varphi \geq \tilde{\varphi}_{\rm onset}$, the MSD shows an inflection point, i.e., a point where $\frac{d^2 \ln \Delta(t)}{(d\ln t)^2} = 0$. In this regime a non-Fickian behavior is observed. Hence, $\tilde{\varphi}_{\rm onset}$ also corresponds to the density at which the minimum value of the non-Fickian coefficient $\nu_{\rm min}$ is unity (Fig. 8d), where $\nu_{\rm min} = \min_t \nu(t)$ and the non-Fickian coefficient $\nu(t) \equiv \frac{d\ln\Delta(t)}{d\ln t}$ [65]. Note, however, that our estimate of $\tilde{\varphi}_{\rm onset}$ likely underestimates the onset calculated from the emergence of a finite configurational entropy in static calculations [66].
- $\varphi_{\rm SER}$ – characteristic density for the breakdown of the Stokes-Einstein relation (SER). Below $\varphi_{\rm SER}$, hopping is irrelevant because, if present, it is indistinguishable from the regular liquid dynamics, and the MCT scaling relations are satisfied (Sec. B 2 a); above $\varphi_{\rm SER}$, hopping becomes faster than the characteristic MCT time ($\tau_{\rm h} < \tau_D$), and consequently both the MCT scaling and the SER are violated.

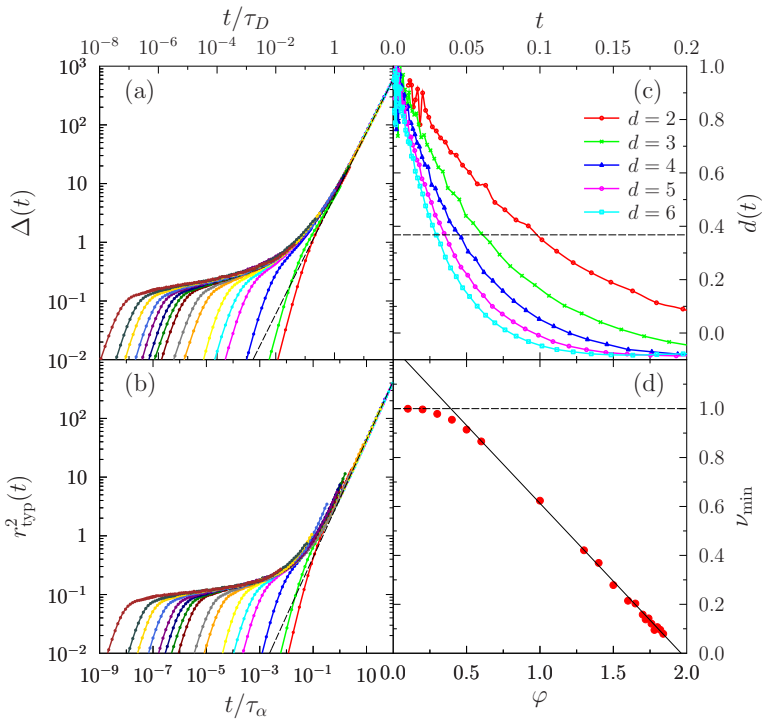

FIG. 8: Rescaled plots of (a) the MSD and (b) the typical displacement $r^2_{\rm typ}(t)$ in $d = 3$. From right to left, $\varphi = 0.40, 0.60, 1.00, 1.30, 1.40, 1.50, 1.60, 1.65, 1.70, 1.72, 1.74, 1.76, 1.78, 1.80, 1.82, 1.84$, with τ_α normalized such that $\tau_\alpha \sim \tau_D$ at $\varphi_{\rm SER}$. Note that the rightmost line (red), at $\tilde{\varphi}_{\rm onset}$, does not exhibit any plateau regime. (c) Velocity autocorrelation function $d(t)$ at $\varphi_{\rm SER}$ in $d = 2 - 6$. By definition, $d(\tau_0) = 1/e$ (dashed line). (d) Minimum value of the non-Fickian coefficient $\nu_{\rm min}$ in $d = 3$. At high densities the $\nu_{\rm min}$ decreases linearly with φ (solid line), and at low densities $\nu_{\rm min} = 1$ (dashed line). The crossover occurs around $\tilde{\varphi}_{\rm onset} = 0.40(5)$.

- $\varphi_{\rm d}$ – dynamical glass transition threshold. In the MK model, this density is theoretically calculated from the replica method (Sec. B 1 c), and numerically confirmed by testing the MCT scaling $\tau_D \sim |\varphi - \varphi_{\rm d}|^{-\gamma}$ (or equivalently, $D \sim |\varphi - \varphi_{\rm d}|^{\gamma}$) in the density range over which hopping is negligible ($\tilde{\varphi}_{\rm onset} < \varphi < \varphi_{\rm SER}$). In the HS model, however, we lack reliable theoretical predictions for $\varphi_{\rm d}$ in low dimensions. We therefore determine $\varphi_{\rm d}$ from fitting the simulation results for D in the regime $\tilde{\varphi}_{\rm onset} < \varphi < \varphi_{\rm SER}$. Our results are consistent with those reported in Ref. [38], where $\varphi_{\rm d}$ was extrapolated from slowly quenching the fluid. Note that $\varphi_{\rm d}$ is only sharply defined when hopping contributions can be separated without ambiguity. Hence, $\varphi_{\rm d}$ is only well defined in the replica calculation, where hopping is excluded by construction.

- $\tilde{\varphi}_{\rm d}$ – effective dynamical glass transition threshold. Empirically, $\tilde{\varphi}_{\rm d}$ is determined by fitting the diffusivity data, as is commonly done in glass formers. In this study we show, however, that $\tilde{\varphi}_{\rm d}$ is systematically shifted with respect to $\varphi_{\rm d}$ ($\tilde{\varphi}_{\rm d} > \varphi_{\rm d}$). Note that because $\tilde{\varphi}_{\rm d}$ is a fitting parameter, it also depends on the density range one chooses (or is available) for the power-law fit.

- $\tilde{\varphi}_0$ – phenomenological parameter from the Vogel-Tammann-Fulcher (VTF) fit to $\tau_D \sim e^{B_{\rm VTF}/(\tilde{\varphi}_0 - \varphi)}$. In the MK model, $\tilde{\varphi}_0$ is clearly different from the thermodynamic Kauzmann transition point $\varphi_K = \infty$. Recall, however, that the MK model lacks the glass-glass nucleation processes assumed by the Adam-Gibbs (AG) and the random first-order transition (RFOT) theories, in order to associate the divergence of the relaxation timescale with the thermodynamic singularity at φ_K.

- $\varphi_{\rm p}$ – percolation threshold for the cage network. Below $\varphi_{\rm p}$, a particle can diffuse by successive hops on the percolating network of cages. Because the infinite time limit of the MSD is only truly bounded above this threshold, $\varphi_{\rm p}$ also provides a upper bound for $\varphi_{\rm d}$, i.e., $\varphi_{\rm p} > \varphi_{\rm d}$.

- $\varphi_{\rm K}$ – Kauzmann transition. Density at which the complexity Σ (or configurational entropy) vanishes. As discussed above, because $\Sigma_{\rm MK} \sim \Sigma_{\rm HS} + \ln N$, the density of the Kauzmann transition diverges ($\varphi_K = \infty$) in the thermodynamic limit.

TABLE I: Numerical values of characteristic densities and MCT exponents for the MK and the HS models.

	d	$\tilde{\varphi}_{\rm onset}$	$\varphi_{\rm SER}$	$\varphi_{\rm d}$	$\tilde{\varphi}_{\rm d}$	$\tilde{\varphi}_0$	γ	$\tilde{\gamma}$	a	b	λ
MK	2	0.50(5)	2.0(1)	2.398	2.60(1)	3.2(1)	4.59(4)	5.77(4)	0.19	0.26	0.92
	3	0.40(5)	1.60(5)	1.776	1.93(1)	2.15(5)	3.27(7)	4.95(4)	0.25	0.40	0.85
	4	0.30(5)	1.10(5)	1.184	1.276(2)	1.40(2)	2.9(1)	4.50(7)	0.28	0.46	0.80
	5	0.20(5)	0.70(2)	0.741	0.783(1)	0.865(5)	2.67(8)	4.04(6)	0.29	0.52	0.78
	6	0.10(5)	0.42(1)	0.445	0.466(1)	0.510(5)	2.65(8)	3.75(4)	0.30	0.53	0.76
HS	3	0.46(2)	0.555(5)	0.5770(5)	0.5885(5)	0.603(1)	1.72(3)	2.8(1)	0.40	1.05	0.47
	4	0.293(6)	0.389(6)	0.4036(2)	0.4069(1)	0.417(1)	1.92(3)	2.26(4)	0.37	0.86	0.57
	5	0.19(2)	0.260(5)	0.2683(1)	0.2699(1)	0.277(1)	1.95(3)	2.23(6)	0.37	0.84	0.58
	6	0.11(1)	0.168(4)	0.1723(1)	0.1731(1)	0.178(1)	2.00(3)	2.22(6)	0.36	0.80	0.60
	7	0.065(5)	0.106(2)	0.1076(1)	0.1081(1)	0.112(1)	2.0(1)	2.23 (7)	0.36	0.80	0.60
	8	0.040(2)	-	0.06585(5)	0.06585(5)	0.0685(5)	2.15(5)	2.15(5)	0.34	0.71	0.65

Data for the MK model in $d = 2 - 6$ and for the HS model in $d = 3 - 8$. Theoretical results are reported for $\varphi_{\rm d}$ of the MK model, but all the other values are from simulations. In $d = 8$ for the HS model, no SER violation is detected in the dynamical regime that is computationally accessible.

Appendix B: Caging

1. Thermodynamics: the caging order parameter and the dynamic transition density

The mean caging order parameter can be obtained equivalently from the replica method, following Refs. [8, 67], or from the cavity method, following Ref. [45]. Here we briefly describe how these approaches are adapted to the MK model.

a. Calculation of the mean caging order parameter: the replica method

References [8, 67] used the replica approach to obtain HS results, and it is straightforward to check that these derivations only rely on the pair correlation function in the liquid phase; terms corresponding to third- and higher-order structural correlations are neglected. The treatment of Ref. [8] can therefore be directly applied to the MK model, for which these assumptions are exact. The results from Ref. [67] have also been obtained using the approximation $g_2(r) = y_{\rm liq}^{\rm HS}(\varphi)\theta(r-\sigma)$, see [67, Eq.(21)] (the soft-sphere temperature is set to zero to study hard-core systems). Comparing this result with Eq. (A2), we see that for the MK model $y_{\rm liq}^{\rm HS}(\varphi) = 1$. All the results of Refs. [8, 67] can thus be straightforwardly extended to the MK model by setting $y_{\rm liq}^{\rm HS}(\varphi) = 1$. (Note that the discussion of Ref. [67] was restricted to $d = 3$, but a general discussion for all d can be found in Ref. [8]). The replicated entropy thus has the form

$$\begin{aligned}
\mathcal{S}(m, A; T, \varphi) &= S_h(m, A) + S_{\rm liq}^{\rm MK}(\varphi) + 2^{d-1}\varphi G(m, A) \ , \\
S_h(m, A) &= \frac{d}{2}(m-1)\ln(2\pi A) + \frac{d}{2}(m - 1 + \ln m) \ , \\
G(m, A) &= d\int_0^\infty dr r^{d-1}[q_A(r)^m - \theta(r-\sigma)] \ , \\
q_A(r) &= \int d\mathbf{r}' f_{2A}^{\rm G}(\mathbf{r}')\theta(|\mathbf{r}-\mathbf{r}'|-\sigma) = \int_D^\infty du \left(\frac{u}{r}\right)^{\frac{d-1}{2}} \frac{e^{-\frac{(r-u)^2}{4A}}}{\sqrt{4\pi A}} \left[e^{-\frac{ru}{2A}}\sqrt{\pi\frac{ru}{A}} I_{\frac{d-2}{2}}\left(\frac{ru}{2A}\right)\right] \ ,
\end{aligned} \tag{B1}$$

where $f_A^{\rm G}(r)$ is the d-dimensional Gaussian cage given in Eq. (A11) and $I_n(x)$ is the modified Bessel function. The last expression for $q_A(r)$ is obtained using bipolar coordinates to compute the convolution [8]. Remarkably, in odd dimensions the integral over u can be computed analytically, which facilitates the numerical evaluation of the replicated entropy.

From Eq. (B1), we can derive the equation for A from the condition $\partial\mathcal{S}/\partial A = 0$, which reads

$$1 = \frac{2^d\varphi}{d}\frac{A}{1-m}\frac{\partial G(m,A)}{\partial A} \equiv \frac{2^d\varphi}{d}F(m,A)\ . \tag{B2}$$

The cage radius in the liquid can be obtained by solving this equation in the limit $m \to 1$, and $\bar{\Delta} = 2dA$. From Eq. (B2), one sees that the dynamical transition $\varphi_{\rm d}$ corresponds to the point where $\frac{2^d\varphi}{d}\max_A F(1,A) = 1$. Note that for $\varphi > \varphi_{\rm d}$ Eq. (B2) admits two solutions, but only the smaller of the two is a stable physical solution [8].

b. Calculation of the cage size distribution: the cavity method

More information on the distribution of individual cage shapes and sizes can be obtained from the cavity method [61, 68]. Its application to the MK model has been developed in Ref. [45], where the cavity equations are derived and discussed. Here, we only present the main steps.

a. **Cavity fields and replica symmetric cavity equations** – In the cavity approach, the system is described by a set of cavity fields $\psi(\mathbf{r})$. Each cavity field describes the probability of finding a particle at position $\mathbf{r}$, when it is added to a system of $N-1$ particles. The replica symmetric cavity equations provide a recurrence equation for determining these cavity fields

$$\begin{aligned}\psi_0(\mathbf{r}_0) &= \frac{1}{z_0}\prod_{j=1}^{N_0}\left[\int d\mathbf{r}_j\psi_j(\mathbf{r}_j)\chi(\mathbf{r}_0-\mathbf{r}_j+\mathbf{\Lambda}_{0j})\right]\ ,\\ z_0 &= \int d\mathbf{r}_0\prod_{j=1}^{N_0}\left[\int d\mathbf{r}_j\psi_j(\mathbf{r}_j)\chi(\mathbf{r}_0-\mathbf{r}_j+\mathbf{\Lambda}_{0j})\right]\ .\end{aligned} \tag{B3}$$

In this recurrence, the new particle interacts with the N_0 other particles, each described by its own cavity field $\psi_j(\mathbf{r}_j)$. The interaction is given by the hard-core constraint $\chi(\mathbf{r}) = e^{-\beta U(r)} = \theta(r-\sigma)$. In this equation the quenched random variables $\mathbf{\Lambda}_{0j}$ are the random shifts that appear in the Hamiltonian, but they should be independently extracted at each cavity iteration. They are independently distributed in the whole volume V with a uniform distribution $P(\mathbf{\Lambda}_{0j}) = 1/V$. Note that in Ref. [45], the cavity equations were obtained for a model defined on a random graph that is locally tree-like, corresponding to a situation where N_0 remains finite as $N \to \infty$. The method, however, is also applicable to the MK model, where $N_0 = N-1$, corresponding to the fully connected graph [61]. A convenient way to obtain the fully connected graph is to first take the limit $N \to \infty$ and then $N_0 \to \infty$. One can show that this procedure is indeed equivalent to considering $N_0 = N-1$ [61].

b. **Translational invariance and irrelevance of the random shifts** – In order to describe the liquid and the glassy states of the MK model, we are interested in solutions of the cavity equation that have statistical translational invariance. To be more precise, the liquid phase is described by uniform fields $\psi(\mathbf{r}) = 1/V$ for all particles. Physically, this situation corresponds to particles diffusing everywhere within the system volume, which mathematically reproduces the virial expansion [45]. In the glass phase, each individual cavity field has the form $\psi(\mathbf{r}) = f_A(\mathbf{r}-\mathbf{R})$, where $f_A(\mathbf{r})$ is a cage function localized around $\mathbf{r} = 0$. The cavity field is thus localized around point $\mathbf{R}$, but the localization centers $\mathbf{R}$ themselves must be uniformly distributed in the whole volume because the glass is globally translationally invariant. Hence, in Eq. (B3), when neighbors are picked at random, they are localized around uniformly distributed random positions in space, which makes the random shifts redundant. In the following, we can thus neglect the random shifts and write the replica symmetric cavity equations as

$$\begin{aligned}\psi_0(\mathbf{r}_0) &= \frac{1}{z_0}\prod_{j=1}^{N_0}\left[\int d\mathbf{r}_j\psi_j(\mathbf{r}_j)\chi(\mathbf{r}_0-\mathbf{r}_j)\right]\ ,\\ z_0 &= \int d\mathbf{r}_0\prod_{j=1}^{N_0}\left[\int d\mathbf{r}_j\psi_j(\mathbf{r}_j)\chi(\mathbf{r}_0-\mathbf{r}_j)\right]\ ,\end{aligned} \tag{B4}$$

and take $N_0 \to \infty$.

c. **The glass phase and the 1RSB cavity equations** – In the glass phase, as mentioned above, $\psi(\mathbf{r})$ are random variables described by a probability distribution $Q[\psi]$. In the regime that is here of interest, the glass is described by the 1RSB cavity equations derived in Refs. [61, 68]. From these equations, we obtain that the probability

distribution $Q[\psi]$ satisfies the self-consistent equation

$$\begin{aligned} Q[\psi_0] &= \frac{1}{\mathcal{Z}_0(m)} \int \prod_{j=1}^{N_0} dQ[\psi_j]\, z_0^m\, \delta\big[\text{Eq. (B4)}\big] \ , \\ \mathcal{Z}_0(m) &= \int \prod_{j=1}^{N_0} dQ[\psi_j]\, z_0^m \ , \end{aligned} \tag{B5}$$

which makes explicit that the N_0 cavity fields describing the neighborhood of the new particle are extracted independently from $Q[\psi]$. The new cavity field is constructed according to Eq. (B4) and weighted according to z_0^m. Note that z_0 is the free volume associated with the new particle, and therefore, by varying the free parameter m, one can select glassy states according to their free volume or, equivalently, their internal entropy.

d. **Reconstruction equations** – Beyond the dynamical transition, ergodicity is broken in the liquid phase, which corresponds to the liquid splitting into many distinct glassy states. It is well known, however, that if configurations are sampled with the equilibrium Gibbs-Boltzmann measure, then the entropy and pressure are analytic around $\varphi_{\rm d}$ and the equilibrium glass phase is the analytical continuation of the liquid phase. In order to weight glassy states according to the equilibrium Gibbs-Boltzmann measure, one has to weight them proportionally to their free volume, hence one must set $m = 1$ [68]. In the case $m = 1$, the 1RSB equations greatly simplify thanks to a mapping onto the reconstruction formalism [42]. Reconstruction is then done by introducing new fields $R_{\mathbf{r}}[\psi(\mathbf{r}')] \equiv \psi(\mathbf{r})Q[\psi(\mathbf{r}')]$. This change of variable ensures that only the fields that are localized around point $\mathbf{r}$ contribute to $R_{\mathbf{r}}[\psi]$. Using the global translational invariance $R_{\mathbf{r}}[\psi(\mathbf{r}')] = R_{\mathbf{0}}[\psi(\mathbf{r}' - \mathbf{r})]$, we conveniently get

$$\begin{aligned} R_0[\psi(\mathbf{r}_0)] &= \int \prod_{j=1}^{N_0} \left[\frac{d\mathbf{r}_j \chi(\mathbf{r}_j)}{\int d\mathbf{r}' \chi(\mathbf{r}')} \right] \int dR_0[\psi_j(\mathbf{r}'_j)]\, \delta\big(\star\big) \ , \\ \star \quad &\leftarrow \quad \psi(\mathbf{r}_0) - \frac{1}{z_0} \prod_{j=1}^{N_0} \left[\int d\mathbf{r}'_j \psi_j(\mathbf{r}'_j) \chi(\mathbf{r}_0 - \mathbf{r}_j - \mathbf{r}'_j) \right] \ . \end{aligned} \tag{B6}$$

Note that the reweighting term z_0^m has now disappeared from the equations. Note also that only $R_0[\psi]$ enters the equations and therefore all cavity fields are localized around the origin. The $\mathbf{r}_j$ in Eq. (B6) are random shifts of the cavity fields that are constrained to be outside a sphere of radius σ around the origin. The neighbors j are thus localized outside that sphere, which guarantees that around the origin there exists a void to accommodate an additional particle.

e. **Ansatz on the cage shape** – As discussed in Ref. [45], numerically solving the cavity equations in Eq. (B6) remains a formidable task. Here, we make a simple ansatz on the cage shape to facilitate this computation. We first assume that the cavity fields all have the form $\psi_j(\mathbf{r}) = f_{A_j}(\mathbf{r} - \mathbf{R})$, where f is a fixed (spherically symmetric) cage shape. We then choose either a Gaussian (Eq. (A11)) or a ball (Eq. (A12)) cage shape, with Δ_i given by Eqs. (A13) and (A14), respectively. We assume that the cage sizes are distributed according to a function $P_f(A)$ while the centers $\mathbf{R}$ are uniformly distributed within the volume, as discussed above. We therefore obtain the ansatz

$$\begin{aligned} Q[\psi(\mathbf{r})] &= \int dP_f(A) \int \frac{d\mathbf{R}}{V} \delta[\psi(\mathbf{r}) - f_A(\mathbf{r} - \mathbf{R})] \ , \\ R_0[\psi(\mathbf{r})] &= \psi(0) Q[\psi(\mathbf{r})] = \int dP_f(A) \int \frac{d\mathbf{R}}{V} f_A(\mathbf{R}) \delta[\psi(\mathbf{r}) - f_A(\mathbf{r} - \mathbf{R})] \ . \end{aligned} \tag{B7}$$

The above equations show that fields contributing to $R_0[\psi]$ are localized around a point $\mathbf{R}$ that is distributed according to $f_A(\mathbf{r})$, and hence $\mathbf{R}$ is itself localized close to the origin. Plugging this ansatz in Eq. (B6), we obtain

$$R_0[\psi(\mathbf{r}_0)] = \int \prod_{j=1}^{N_0} \left[\frac{d\mathbf{r}_j \chi(\mathbf{r}_j)}{\int d\mathbf{r}' \chi(\mathbf{r}')} \right] \int dP_f(A_j) \frac{d\mathbf{R}_j}{V} f_{A_j}(\mathbf{R}_j)\ \delta \left[\psi(\mathbf{r}_0) - \frac{1}{z_0} \prod_{j=1}^{N_0} q_{A_j/2}[\mathbf{r}_0 - (\mathbf{r}_j + \mathbf{R}_j)] \right] \ , \tag{B8}$$

where

$$q_A(\mathbf{r}) = \int d\mathbf{r}' f_{2A}(\mathbf{r}') \chi(\mathbf{r} - \mathbf{r}') \tag{B9}$$

Note that the factor of 2 is introduced to follow the notational convention of Ref. [8].

f. **Reconstruction procedure** – The physical interpretation of the reconstruction equation is quite straightforward. In order to construct a new cavity around the origin, one should draw at random $N_0 \to \infty$ particles that are located at random positions $\mathbf{r}_j$ outside a sphere of radius σ around the origin. These particles are themselves within a cage, whose size A_j is extracted from $P_f(A)$. The point $\mathbf{r}_j$ is *not* the center of the cage, but a point that is typical of the distribution inside the cage. The cage center is therefore at $\mathbf{r}_j+\mathbf{R}_j$, where the shift $\mathbf{R}_j$ is extracted from the cage shape $f_{A_j}(\mathbf{R}_j)$. Each neighbor rattles around its cage center at $\mathbf{r}_j + \mathbf{R}_j$, producing an effective potential that convolutes the HS constraint with the cage shape, $e^{-\beta v^j_{\rm eff}(\mathbf{r}_0)} = q_{A_j/2}[\mathbf{r}_0 - (\mathbf{r}_j + \mathbf{R}_j)]$. The new cavity field is then given by the (normalized) exponential of the sum of all effective potentials, $\psi(\mathbf{r}_0) \propto \prod_j q_{A_j/2}[\mathbf{r}_0 - (\mathbf{r}_j + \mathbf{R}_j)] = \exp[-\beta \sum_j v^j_{\rm eff}(\mathbf{r}_0)]$. Finally, we note that although the number of neighbors N_0 should be sent to infinity, distant neighbors do not affect the new cavity field because $q_{A_j/2}(\mathbf{r})$ tends to 1 when $\mathbf{r} \to \infty$. We can therefore introduce an arbitrary spatial cutoff and only consider the neighbors (whose number distribution is Poissonian) that are within this cutoff, and then increase the cutoff until the results converge. This approach is expressed by the following recursive procedure for self-consistently determining the distribution $P_f(A)$, which is the only remaining unknown in the cavity reconstruction. Note that once $P_f(A)$ has been calculated, one can easily obtain the distribution of mean square displacements in the cage, $P_f(\Delta)$, according to Eq. (A13) or (A14). This observable is also easily measured in numerical simulations (and experiments).

Procedure-Reconstruction-MK

1. Consider a spherical shell $\sigma < r < \sigma + \sigma_{\rm cut}$ of volume V_0 (the upper bound $\sigma_{\rm cut}$ should be sufficiently large for the results to be independent of it). Consider a number of centers N_0 distributed according to a Poisson law with average $\overline{N_0} = \rho V_0$. Uniformly draw these sphere centers $\mathbf{r}_j$ within the shell.

2. Independently draw N_0 cage radii A_j from $P_f(A)$, and N_0 displacements $\mathbf{R}_j$ from $f_{A_j}(\mathbf{R}_j)$.

3. From these N_0 random variables, derive a new cavity field

$$\psi(\mathbf{r}_0) = \frac{\prod_{j=1}^{N_0} q_{A_j/2}(\mathbf{r}_0 - (\mathbf{r}_j + \mathbf{R}_j))}{\int d\mathbf{r}'_0 \prod_{j=1}^{N_0} q_{A_j/2}(\mathbf{r}'_0 - (\mathbf{r}_j + \mathbf{R}_j))} \ . \tag{B10}$$

4. Compute the mean square displacement in the new cavity as

$$\begin{aligned} \langle \mathbf{r}_0 \rangle &= \int d\mathbf{r}_0 \, \mathbf{r}_0 \, \psi(\mathbf{r}_0) \\ \langle \delta \mathbf{r}_0^2 \rangle &= \int d\mathbf{r}_0 \, (\mathbf{r}_0 - \langle \mathbf{r}_0 \rangle)^2 \, \psi(\mathbf{r}_0) = \Delta_{\rm new}/2 \ . \end{aligned} \tag{B11}$$

   The value $\Delta_{\rm new}$ is the long-time mean square displacement corresponding to Eq. (A10). It allows one to determine the new cage parameter $A_{\rm new}$ that enters in the new cage shape in Eq. (A11) (or (A12)), according to Eq. (A13) (or (A14)).

5. Repeat steps (1-4) to get $\mathcal{N}$ samples $A_{\rm new}$ in order to construct a new distribution $P_f(A_{\rm new})$.

6. Repeat (5) until the distribution converges $P_f(A_{\rm new}) \simeq P_f(A)$ within the statistical error.

7. From the convergent $P_f(A)$ compute the distribution of mean square displacements, $P_f(\Delta)$, using Eq. (A13) (or (A14)).

---

g. **Numerical details** – In principle, the above procedure provides a theoretical way to compute $P_f(A)$, but practically it must be implemented numerically, with two additional tricks.

First, we note that it is difficult to calculate the normalization of the cavity field $\psi(\mathbf{r}_0)$ in Eq. (B10), because one has to integrate over the whole space. It is more convenient to compute the variance $\langle \delta \mathbf{r}_0^2 \rangle$ in Eq. (B11) using the Metropolis algorithm without explicitly obtaining $\psi(\mathbf{r}_0)$. We can then write Eq. (B10) as

$$\psi(\mathbf{r}_0) = \frac{\tilde{\psi}(\mathbf{r}_0)}{\int d\mathbf{r}_0 \tilde{\psi}(\mathbf{r}_0)}, \tag{B12}$$

where the non-normalized probability $\tilde{\psi}(\mathbf{r}_0)$ is

$$\tilde{\psi}(\mathbf{r}_0) \equiv \prod_{j=1}^{N_0} q_{A_j/2}[\mathbf{r}_0 - (\mathbf{r}_j + \mathbf{R}_j)]. \tag{B13}$$

From this expression, it is clear that $\tilde{\psi}(\mathbf{r}_0)$ is analogous to the Boltzmann factor in the Gibbs measure with an effective potential $\mathcal{H}_{\rm eff}(\mathbf{r}_0)$, $\tilde{\psi}(\mathbf{r}_0) = e^{-\beta\mathcal{H}_{\rm eff}(\mathbf{r}_0)}$. We can thus use the standard Monte Carlo (MC) algorithm to sample any average quantity, such as $\langle \delta\mathbf{r}_0^2 \rangle$, with acceptance rate

$$\mathrm{acc}(\mathbf{r}_0^{\rm old} \to \mathbf{r}_0^{\rm new}) = \min\{1, \tilde{\psi}(\mathbf{r}_0^{\rm new})/\tilde{\psi}(\mathbf{r}_0^{\rm old})\}. \tag{B14}$$

Interestingly, we actually derived from the cavity formalism a "local" MC simulation. In this local MC sampling, the positions of all the particles, except for the caged particle at $\mathbf{r}_0$, are fixed and their vibrational contribution to the motion of the caged particle is integrated into the effective potential $\mathcal{H}_{\rm eff}(\mathbf{r}_0)$. In our simulations, we perform 4×10^5 MC steps with step size $0.1\sqrt{\bar{A}}$ to calculate each cage size.

Second, we have to remove hopping from the cavity procedure, or otherwise the cavity solution does not properly converge (see Fig. 9). To achieve this task, during the calculation of $A_{\rm new}$ in the local MC simulations, we record the spatial trajectory of $\mathbf{r}_0$. We then check if any hopping occurs during this trajectory using the detection algorithm described in Sec. C 1. We only include $A_{\rm new}$ in the statistics of $P_f(A_{\rm new})$ if no hopping is detected, as otherwise the particle is not truly caged. Once hopping is removed, our results indicate that the cavity solution properly converges when $\varphi > \varphi_{\rm d}$ (see Fig. 9). We represent the distribution $P_f(A)$ by a number $\mathcal{N} = 10^4 \gg \overline{N_0}$ of samples A_k, $k = 1 \cdots \mathcal{N}$.

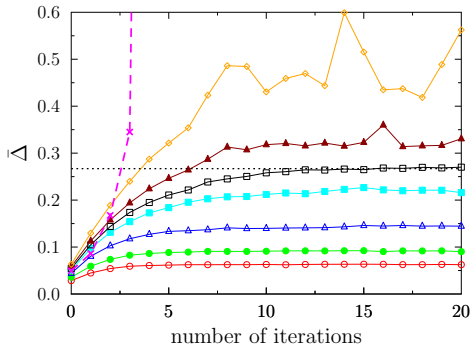

FIG. 9: Evolution of mean square displacement $\bar{\Delta}$ under iteration of the cavity reconstruction, at (solid lines, from bottom to top) $\varphi = 2.50, 2.20, 1.95, 1.80, 1.75, 1.70, 1.60$ in $d = 3$. The solution becomes completely unstable above $\Delta_d = 0.267$ (dotted black line), as predicted by the replica method. If hopping is not removed, the solution diverges quickly when φ approaches $\varphi_{\rm d}$. See, for instance, the unfiltered results for $\varphi = 1.95$ (pink dashed line).

c. *Comparing theoretical predictions with simulations*

We first show that the mean square displacement $\bar{\Delta}$ predicted from both the replica and the cavity methods is generally in good agreement with the simulation data (Fig. 10). The simulation $\bar{\Delta}$ is extracted from the asymptotic time limit of the MSD data, according to the MCT scaling (see Eq. (B21) below). Close to $\varphi_{\rm d}$, the replica theory predicts a scaling (Fig. 10)

$$|\bar{\Delta}(\varphi) - \Delta_{\rm d}| \sim |\varphi - \varphi_{\rm d}|^{1/2} , \tag{B15}$$

where $\Delta_{\rm d} = \bar{\Delta}(\varphi_{\rm d})$, that is consistent with the MCT prediction. However, around $\varphi_{\rm d}$ precisely determining $\bar{\Delta}$ from either simulations or cavity reconstruction requires a careful consideration of hopping. The simulation and the cavity data therefore unsurprisingly deviate from Eq. (B15) in that regime (Fig. 10).

Cavity reconstruction provides a theoretical prediction for the distribution $P_f(\Delta)$ of individual mean square displacements. In order to obtain individual cages from simulation, we use Eq. (A10) at $t = 2$, which is sufficiently long for the cages to form, but not so long that a large fraction of particles have hopped. Note that at densities well above

$\varphi_{\rm d}$, hopping is so rare that this choice of timescale is irrelevant. As discussed in the main text, our theoretical results agree well with simulations, and are independent of the Gaussian or of the ball ansatz for the shape functional. The replica calculation for $\bar{\Delta}$ using the Gaussian functions and $P_f(\Delta) = \delta(\Delta - \bar{\Delta})$ also agrees with the simulation results (Fig. 10).

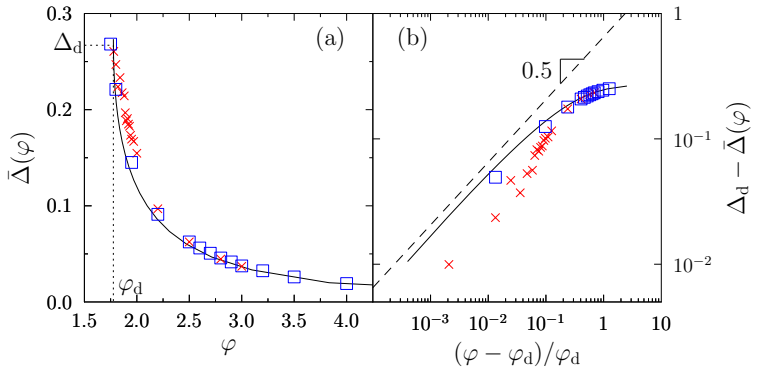

FIG. 10: (a) The $d = 3$ mean square displacement $\bar{\Delta}(\varphi)$ obtained from replica method (black line), cavity reconstruction (blue squares), and MD simulations (red crosses). The replica result for $\varphi_{\rm d}$ correspond to the point where the theoretical replica line has a square root singularity. (b) The theoretical results are consistent with the scaling form in Eq. (B15), but deviations are observed in the MD data close to $\varphi_{\rm d}$, due to the ambiguity in determining cage sizes when hopping is significant.

In summary, we find a basic consistency between our MD simulations and theoretical calculations, including (i) the replica calculation with a Gaussian anzatz for the cage shape and a δ-function approximation for the cage size distribution function $P_f(\Delta) \approx \delta(\Delta - \bar{\Delta})$, and (ii) the cavity method with both Gaussian and ball anzatzs. It has been shown that in the limit $d \to \infty$, the theoretical result (of replica calculation) is independent of the cage shape anzats [10], and we also expect it to be independent of the method we use (replica/cavity). In finite dimensions, weak dependence is expected, but according to our results presented here, it is insignificant compared to the numerical accuracy of the resolution of the cavity equations.

2. Caging dynamics: mode-coupling theory (MCT) and beyond

In this section, we compare the MD results with the dynamical caging behavior predicted by MCT. The MCT scalings are found to only be consistent with our data when $\varphi < \varphi_{\rm SER}$. Above $\varphi_{\rm SER}$, MCT predictions are violated, which is well captured by the breakdown of SER and is a consequence of entangling caging with hopping, as discussed in Sec. C. It is important to note that we here only refer to MCT as the general scaling laws predicted by the schematic MCT equation [6], which can be also independently derived from the static framework [69]. The traditional MCT kernel being incorrect for the MK model [44], the numerical MCT predictions are indeed unsuitable for comparison.

a. Testing the mode-coupling theory

We first compile the MCT predictions tested in our study. The derivations of these predictions as well as many important physical interpretations can be found in Ref. [6] and references therein. We denote $\epsilon = \frac{\varphi - \varphi_{\rm d}}{\varphi_{\rm d}}$ as the distance from the dynamical transition, and τ_ϵ as the characteristic time for the β-relaxation. Note that MCT does not predict any breakdown of the SER, so we do not distinguish between the α-relaxation time τ_α and the diffusion time τ_D in this analysis ($\tau_D \sim \tau_\alpha \gg \tau_\epsilon$). Below the dynamical transition $\varphi < \varphi_{\rm d}$, MCT predicts that the time evolution of the MSD has the form

$$\Delta_-(t) = \begin{cases} \Delta_d - B|\epsilon|^{1/2} \left(\frac{t}{\tau_\epsilon}\right)^{-a}, & t \ll \tau_\epsilon, \\ \Delta_d + C \left(\frac{t}{\tau_D}\right)^b + \frac{t}{\tau_D}, & t \gg \tau_\epsilon, \end{cases} \tag{B16}$$

where B and C are density-independent constants, and the exponents a and b are related by the exponent parameter λ as

$$\lambda = \frac{[\Gamma(1-a)]^2}{\Gamma(1-2a)} = \frac{[\Gamma(1+b)]^2}{\Gamma(1+2b)}. \tag{B17}$$

Equation (B16) shows that the relaxation process of Δ can be divided into three regimes: (i) an early β-relaxation towards the plateau Δ_d, $\Delta_d - \Delta_-(t) \sim t^{-a}$, (ii) a late β-relaxation leaving from the plateau, $\Delta_-(t) \sim t^b$, and (iii) a diffusive process that is linear in time $\Delta_-(t) \sim t$. We stress that, as described in Sect. A 3 a, before regime (i), there is a ballistic regime characterized by a microscopic time that is much smaller than τ_ϵ and is not included in Eq. (B16).

One of the most important predictions made by MCT is that, upon approaching $\varphi_{\rm d}$, a power-law divergence should be observed for

$$\tau_D \sim |\varphi - \varphi_{\rm d}|^{-\gamma}, \tag{B18}$$

and

$$\tau_\epsilon \sim |\varphi - \varphi_{\rm d}|^{-1/2a}, \tag{B19}$$

where the exponents are related via

$$\gamma = \frac{1}{2a} + \frac{1}{2b}. \tag{B20}$$

Beyond $\varphi_{\rm d}$, MCT then predicts

$$\Delta_+(t) = \begin{cases} \Delta_{\rm d} - B|\epsilon|^{1/2} \left(\frac{t}{\tau_\epsilon}\right)^{-a}, & t \ll \tau_\epsilon \ , \\ \Delta_{\rm d} \ , & t \gg \tau_\epsilon \ . \end{cases} \tag{B21}$$

These scalings are tested by the following procedure.

Procedure-Testing-MCT

1. Obtain $\varphi_{\rm d}$ and $\Delta_{\rm d}$ from the replica calculation.

2. Fit τ_D according to Eq. (B18) (see Fig. 1 of main paper) with the theoretical $\varphi_{\rm d}$, in order to obtain the exponent γ. A consistent power-law scaling is only observed below some density $\varphi_{\rm SER}$; above $\varphi_{\rm SER}$, τ_D becomes smaller than the MCT predictions, implying that an additional relaxation process starts to interfere with the dynamics. This observation suggests that when we fit the diffusivity data, only the data below $\varphi_{\rm SER}$ should be used. If instead we treat $\varphi_{\rm d}$ as a fitting parameter for the entire density range, then we end up with shifted values $\tilde{\varphi}_{\rm d}$ and $\tilde{\gamma}$

   $$\tau_D \sim |\varphi - \tilde{\varphi}_{\rm d}|^{-\tilde{\gamma}}, \tag{B22}$$

   From the analysis presented in the main text, it is clear that MCT actually fails when $\varphi > \varphi_{\rm SER}$, and thus the apparent power-law fitting of Eq. (B22) is not reliable. Results for $\varphi_{\rm d}$, $\tilde{\varphi}_{\rm d}$, γ and $\tilde{\gamma}$ can be found in Table I.

3. Determine a and b (Table I) from γ using Eqs. (B17) and (B20).

4. Test the dynamical behavior of $\Delta(t)$ (Eq. (B16)) below $\varphi_{\rm d}$, and determine the constants B and C. Note that here we have fixed all the other parameters, $\varphi_{\rm d}, \Delta_{\rm d}, a$ and b from previous steps. Figure 11(a) and (b) show that when $\varphi < \varphi_{\rm SER}$, Eq. (B16) is satisfied in the entire time regime; when $\varphi < \varphi_{\rm SER}$, it is only satisfied in the early β-relaxation regime.

5. Using the same constant B, check the MCT dynamics above $\varphi_{\rm d}$ using Eq. (B21). When φ is not too far away from $\varphi_{\rm d}$, $\Delta(t)$ does not strictly saturate to a plateau as predicted by MCT, and the scaling behavior of the intermediate time regime is modified.

---

b. Breakdown of the Stokes-Einstein relation

The above analysis shows that the MCT scalings start to break down close to the dynamical transition $\varphi_{\rm d}$. To further investigate this property, we look at the scaling relation between the diffusion time τ_D and the relaxation time

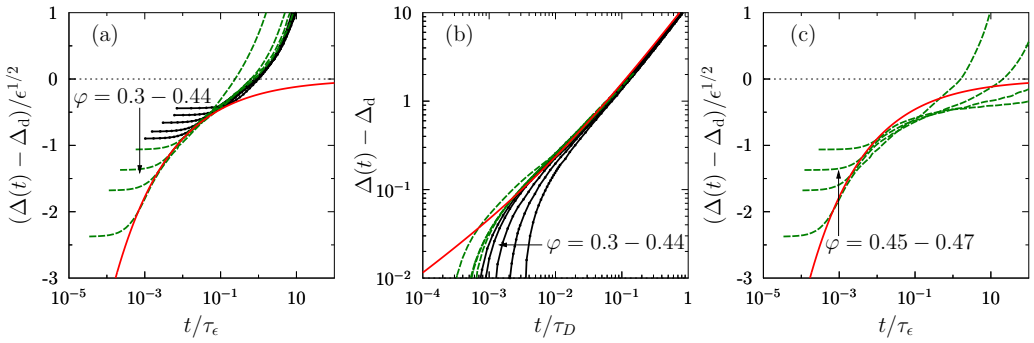

FIG. 11: Testing MCT scalings for the MK model in $d = 6$. Below φ_d, the MD data for $\varphi = 0.30, 0.35, 0.38, 0.40, 0.41, 0.42, 0.43, 0.435, 0.44$ are fitted to Eq. (B16) (red lines) for (a) the early β-relaxation, and (b) the late β-relaxation together with diffusion, using fitting parameters $B = 0.073$ and $C = 1.3$. (c) Above φ_d, the MD data $\varphi = 0.45, 0.455, 0.46, 0.47$ are compared to the early β-relaxation scaling in Eq. (B21) with the same value of B. A good agreement is found for the entire time regime when $\varphi < \varphi_{SER}$ (black solid lines). When $\varphi > \varphi_{SER}$ (green dashed lines), we only observe a good agreement for the early β-relaxation regime, which suggests that at later times hopping mixes with the MCT dynamics.

τ_α. If SER were obeyed, we should obtain $\tau_D \sim \tau_\alpha$. As shown in Fig. 1 in the main paper, SER breaks down when $\varphi > \varphi_{SER}$ as

$$\tau_D \sim \tau_\alpha^{1-\omega}, \tag{B23}$$

where the exponent $\omega = 0.22$ is invariant with d.

The breakdown of SER is beyond the MCT description. Interestingly, we observe that three phenomena happen at the same density φ_{SER}: (i) violation of MCT scalings, (ii) violation of SER, and (iii) the hopping characteristic time τ_h becoming comparable with τ_D. Our interpretation of these observations is presented in the main text.

3. Percolation of the cage network

Because cages can be connected via hopping channels, it is natural to examine how the cages are topologically connected. We find that the network of cages spans the system below density φ_p ($\varphi_p > \varphi_d$). Above φ_p, only local cage clusters are formed and particles become strictly confined. We show that this phenomenon can be mapped onto a void percolation transition, which belongs to the same universality class as regular percolation.

a. Mapping the glass transition to a void percolation transition

To do the mapping, we first consider the simplest case, where we assume that all the neighbors of a given particle are frozen, $P_f(A) = \delta(A)$. We want to know if the caged particle can move to another cage without overlapping with other particles. Equivalently, we can rescale the size of neighbors as $\sigma \to 2\sigma$, and look for a hopping path for the point representing the caged particle in the leftover void space (see Fig. 12a).

We next consider the situation where cage sizes are not zero. In this case, particle j is rattling inside a cage with radius $\sqrt{A_j}$, whose distribution is a density dependent function $P_f(A)$. If a certain channel were closed in the first case, there is now a possibility for it to be open because the particles bounding that channel are now thermally moving. Because we are interested in the upper bound for percolation, i.e., the best case scenario for hopping, we rescale particle sizes as (see Fig. 12a):

$$\sigma \to 2(\sigma - 2\sqrt{A_j}), \tag{B24}$$

where A_j is drawn from $P_f(A)$. If no path in void space is found by this construction, then the particle is confined. Strictly speaking, this procedure only works for cage shapes with sharp boundaries, like the ball function in Eq. (A12). For a Gaussian cage in Eq. (A11), the confined particle always has a finite (but vanishingly small) probability to hop, even if the cage is found to be closed in the percolation mapping. In the following percolation analysis, to avoid any possible confusion, we assume that all cages have ball shapes, which corresponds to assuming that this probability tail is negligible.

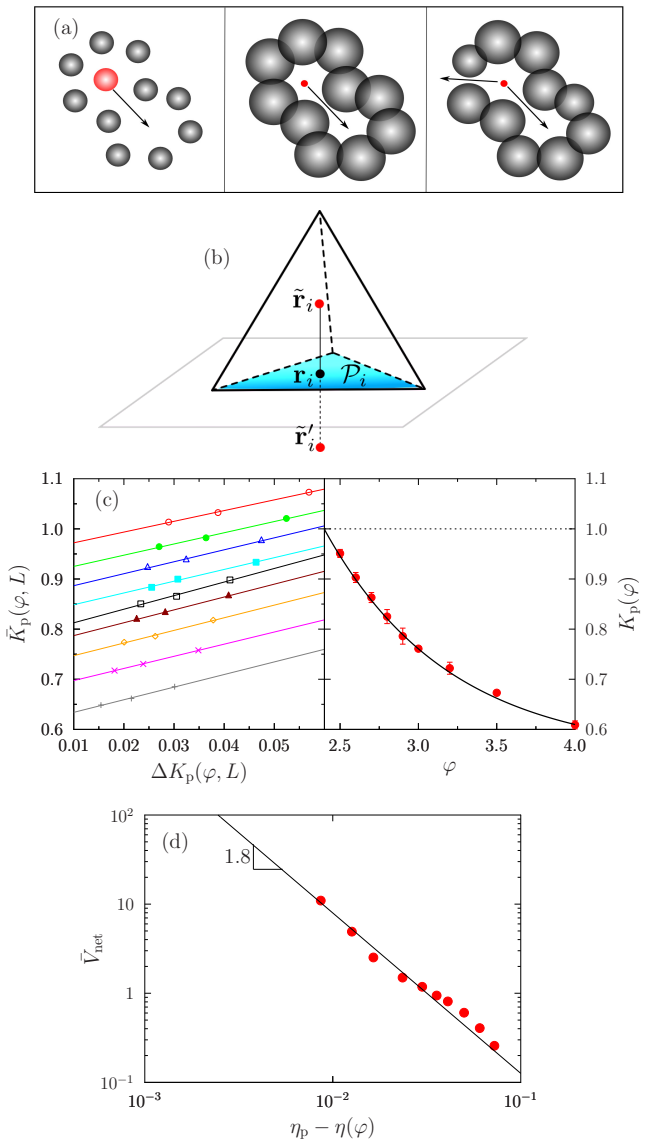

FIG. 12: Percolation analysis. (a) Mapping the glass transition problem to a void percolation transition according to the rescaling law $\sigma \to 2\sigma$ (from left to middle panels), and according to $\sigma \to 2(\sigma - 2\sqrt{A_j})$ (from left to right panels). In the latter case, additional hopping paths may be found. (b) Calculating the radical Voronoi cell $\mathcal{P}_i$ (blue triangle) of sphere i in dimension d ($d = 2$ in this example). The problem is mapped onto a Voronoi tesselation in dimension $d+1$, where the tetrahedron is the Voronoi cell of $\tilde{\mathbf{r}}_i$ in the mapped $d+1$ configuration. (c) Determining φ_p in $d = 3$. Left: estimation of the percolation threshold $K_\mathrm{p}(\varphi)$ from the finite-size analysis of Eq. (B32). Right: determining the percolation density $\varphi_\mathrm{p} = 2.4$ from $K_\mathrm{p}(\varphi_\mathrm{p}) = 1$. The black line is an exponential fit of the data points. (d) Scaling of the mean cluster volume is consistent with Eq. (B33) using the exponent $\gamma_\mathrm{p} = 1.8$ given by standard lattice percolation.

b. Methodology for determining the void percolation threshold

Mapping the void space onto a network via the Voronoi tessellation – For void percolation, unlike for lattice percolation, or for continuous percolation (which is the dual problem to void percolation), the pre-defined network is not trivial to extract. It is has been shown, however, that the void space between monodisperse spheres can be represented by a network obtained by Voronoi tessellation [70]. This method can also be generalized to polydisperese systems via radical Voronoi tessellation [71]. In the network representation, nodes are Voronoi vertices, and links are the edges of the Voronoi polyhedra. If any link passes through one or more sphere, then it is blocked and should be removed from the network. After this network is constructed, we check if there exists a percolated path from the center of the network to the system boundary.

Algorithm for radical Voronoi tessellation of polydisperse spheres in any d– Because our systems have a range of cage sizes, i.e., they map onto spheres with a polydisperse diameters, we develop a method to produce the radical Voronoi tessellation for a given configuration. The basic idea is to map the radical Voronoi tessellation in dimension d to a Voronoi tessellation in dimension $d+1$, and then use Qhull [72] to compute the Voronoi tessellation.

For the standard Voronoi tessellation, the Voronoi cell for sphere i consists of space points $\mathbf{r}$ that satisfy the relation

$$|\mathbf{r}-\mathbf{r}_i| < |\mathbf{r}-\mathbf{r}_j|, \tag{B25}$$

for any $j \neq i$. The radical Voronoi tessellation is a generalization of this definition for unequal sized spheres:

$$|\mathbf{r}-\mathbf{r}_i|^2 - R_i^2 < |\mathbf{r}-\mathbf{r}_j|^2 - R_j^2, \tag{B26}$$

where $R = \sigma/2$ is the particle radius.

In order to map the radical Voronoi tessellation to a Voronoi tessellation, we denote $R_{\max}$ the maximum radius, and introduce a set of points in dimension $d+1$, $\tilde{\mathbf{r}}_i = (\mathbf{r}_i^1, \mathbf{r}_i^2, \ldots, \mathbf{r}_i^d, \sqrt{R_{\max}-R_i^2})$, where $i = 1 \ldots N$. The first d coordinates of $\tilde{\mathbf{r}}_i$ are the same as $\mathbf{r}_i$, and the final coordinate is a function of the sphere radius. We further introduce a set of dual points $\tilde{\mathbf{r}}_i' = (\mathbf{r}_i^1, \mathbf{r}_i^2, \ldots, \mathbf{r}_i^d, -\sqrt{R_{\max}-R_i^2})$, as images of $\tilde{\mathbf{r}}_i$'s with respect to the last coordinates. For each pair $\{\tilde{\mathbf{r}}_i, \tilde{\mathbf{r}}_i'\}$, we find the d-dimensional polygon $\mathcal{P}_i$ that is the common Voronoi boundary between these two points (Fig. 12b). According to the definition in Eq. (B25), it is clear that any point $\tilde{\mathbf{r}}$ in $\mathcal{P}_i$ can be written as $\tilde{\mathbf{r}} = (\mathbf{r}, 0)$, and $\tilde{\mathbf{r}}$ satisfies

$$|\tilde{\mathbf{r}}-\tilde{\mathbf{r}}_i| < |\tilde{\mathbf{r}}-\tilde{\mathbf{r}}_j|, \tag{B27}$$

which is equivalent to

$$|\mathbf{r}-\mathbf{r}_i|^2 + R_{\max}^2 - R_i^2 < |\mathbf{r}-\mathbf{r}_j|^2 + R_{\max}^2 - R_j^2. \tag{B28}$$

Because this relation is exactly the definition of the radical Voronoi cell in Eq. (B26), we have proven that the d-dimensional polygon $\mathcal{P}_i$ is the radical Voronoi cell of sphere i in the original configuration.

Determining the percolation threshold from the scaling theory– The percolation threshold can be determined by finite-size scaling [73]. Note that in the void percolation analysis, the variable of interest is the volume fraction of void space η, and not directly the volume fraction φ [71, 74]. Because our planted configuration is essentially a Poisson process of overlapping spheres, however, we have

$$\eta(\varphi) = \left[1 - \frac{V_d(\sigma/2)}{V}\right]^N \approx e^{-\frac{NV_d(\sigma/2)}{V}} = e^{-\varphi}. \tag{B29}$$

Let $\eta_{\rm p} = e^{-\varphi_{\rm p}}$ be the percolation threshold in the infinite system-size limit. For a system of finite linear size $L \sim V^{1/d}$, the average effective percolation threshold $\bar{\eta}_{\rm p}(L)$ and its variance $\Delta\eta_{\rm p}(L)$ are linearly related [75]

$$|\bar{\eta}_{\rm p}(L) - \eta_{\rm p}| \sim \Delta\eta_{\rm p}(L), \tag{B30}$$

which allows one to numerically determine $\eta_{\rm p}$. Because the polydispersity associated with the cage distribution $P_f(A)$ varies with density φ, we cannot, however, directly use this relation. At each φ, we instead modify the rescaling rule of Eq. (B24) by adding a factor $K(\varphi, L)$

$$\sigma \to 2(\sigma - 2\sqrt{A_j})K(\varphi, L), \tag{B31}$$

and use a binary search to find the percolation threshold $K_{\rm p}(\varphi, L)$ for each configuration. We then calculate $\bar{K}_{\rm p}(\varphi, L)$ and $\Delta K_{\rm p}(\varphi, L)$ over 1000 independent realizations, and use a similar relation

$$|\bar{K}_{\rm p}(\varphi, L) - K_{\rm p}(\varphi)| \sim \Delta K_{\rm p}(\varphi, L), \tag{B32}$$

to determine $K_{\rm p}(\varphi)$ (Fig. 12c). We finally compute $\varphi_{\rm p}$, such that $K_{\rm p}(\varphi_{\rm p}) = 1$. Our system is thus percolated at $\varphi_{\rm p}$, without the extra rescaling factor $K_{\rm p}(\varphi)$ (Fig. 12c).

To check the universality of the percolation transition, we examine the scaling of the mean cluster size $\bar{V}_{\rm net}$, where $V_{\rm net}$ is the total volume of the cluster of cages connected to the planted central cage. According to percolation theory, $\bar{V}_{\rm net}$ diverges at the percolation threshold as a power-law with exponent $\gamma_{\rm p}$:

$$\bar{V}_{\rm net} \sim |\eta(\varphi) - \eta_p|^{-\gamma_p}. \tag{B33}$$

Figure 12d shows that our results are in agreement with $\gamma_{\rm p} = 1.8$ [75] given by lattice percolation, in support of the two problems sharing a same universality class.

Procedure for determining $\varphi_{\rm p}-$ Based on the above discussion, we summarize the procedure for determining $\varphi_{\rm p}$.

Procedure-$\varphi_{\rm p}$-determination

1. For a given density φ, obtain the distribution $P_f(A)$ from the cavity method.
2. Plant a configuration with linear system size L such that the central particle is compatible with all neighbors (this requirement is the same as for the cavity method, see Sec. B 1 b).
3. Rescale the particle sizes following Eq. (B31).
4. Find the percolation threshold $K_{\rm p}(\varphi, L)$ for the configuration using a binary search. To determine if the void space is percolated:
   - Map the d-dimensional configuration of rescaled polydisperse spheres to a $(d+1)$-dimensional configuration of monodisperse spheres.
   - Use a Voronoi protocol to calculate the Voronoi tesselation of the $(d+1)$-dimensional configuration.
   - Map back the $(d+1)$-dimensional Voronoi tesselation to the d-dimensional radical Voronoi tesselation.
   - From the radical Voronoi tesselation, construct a network.
   - Determine if the network is percolated.
5. Repeat (1-4) to get $\bar{K}_{\rm p}(\varphi, L)$ and $\Delta K_{\rm p}(\varphi, L)$.
6. Vary L and repeat (5) to get $\bar{K}_{\rm p}(\varphi, L)$ and $\Delta K_{\rm p}(\varphi, L)$ at different L, and use the finite scaling Eq. (B32) to obtain $K_{\rm p}(\varphi)$.
7. Vary φ and repeat (6) to get $K_{\rm p}(\varphi)$ at different φ, and find $\varphi_{\rm P}$ such at $K_{\rm p}(\varphi_{\rm p}) = 1$.

Appendix C: Hopping

In this section, we detail how we detect hopping events in numerical simulations, and describe the hopping dynamics of the MK model at a phenomenological level. Theoretical investigations are left to future study.

1. Detecting hopping

We follow the algorithm of Refs. [22, 28] to detect hopping events in both the MD simulations and the numerical evaluation of the cavity equations. Below we briefly summarize the procedure.

Procedure-detection-hopping

1. Run simulations and save particle trajectories.
2. Determine the cage size Δ_i of each particle as discussed in Sec. A 3 a. (We relax the assumption of Refs. [22, 28] that all cages have the same size.)
3. Split each single-particle trajectory $X(0 < t < t_{\rm tot})$ into two subsets $X_1(0 < t_1 < t^*)$ and $X_2(t^* < t_2 < t_{\rm tot})$, and measure the mean square distance between the two sub-trajectories

$$\delta(t^*) = \xi(t_c)[\langle d_1(t_2)^2\rangle_{t_2}\langle d_2(t_1)^2\rangle_{t_1}]^{1/2}, \tag{C1}$$

   where $d_j(t_k)$ is the distance between the point at time t_k and the center of mass of the subset X_j $(j,k = 1,2)$, and $\xi(t_c) = \sqrt{\frac{t^*}{t_{\rm tot}}\left(1 - \frac{t^*}{t_{\rm tot}}\right)}$ is a normalization factor. Find the time $t^*_{\rm max}$ such that $\delta(t^*_{\rm max})$ is maximum.

4. For particle i, if $\delta_i(t^*_{\max}) > \Delta_i$, hopping is detected, and the process is repeated recursively for each sub-trajectory until $\delta_i(t^*_{\max}) < \Delta_i$ in each sub-trajectory.

Following this procedure, we save a sequence of hopping times Note that in this study we are only interested in the time of the first hopping, which is equivalent to the time during which the particle is trapped in a cage before escaping. Because facilitation is reduced in the MK model, especially at high φ, we do not specifically distinguish between the first and the subsequent hopping events. The algorithm generally works well at densities $\varphi > \varphi_{\rm d}$, as shown in Fig. 13. Close to $\varphi_{\rm d}$, however, hopping is mixed with other relaxation processes, and cages are not clearly defined. Detecting hopping indeed then becomes more sensitive to the specific cutoff thresholds.

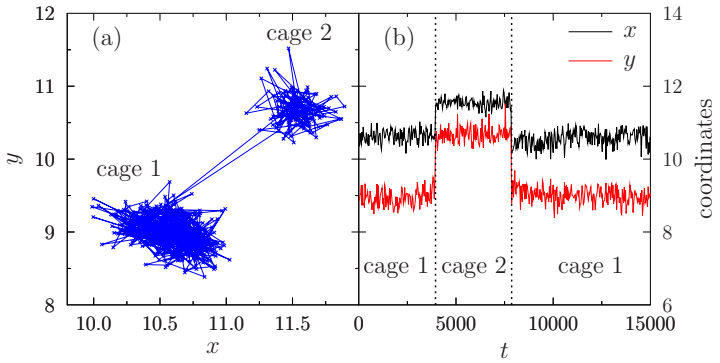

FIG. 13: An example of hopping detection in $d = 2$ at $\varphi = 2.40$. (a) The particle trajectory clearly reveals two well formed cages. (b) The hopping between cages are visualized in the time series, with the two detected hopping times (dotted lines) at $t = 3948.0$ and $t = 7863.6$.

2. Hopping dynamics

Empirically, we find that the above detected hopping time t follows a power-law distribution (see Fig. 3 of the main paper)

$$p_{\rm h}(t) \sim t^{-\mu}, \tag{C2}$$

with exponent $\mu < 1$. We can write its cumulative distribution function as

$$G_{\rm h}(t) = (t/\tau_{\rm h})^{1-\mu}, \tag{C3}$$

where $\tau_{\rm h}$ is the characteristic hopping time scale, representing the time needed for all particles to hop, $G_{\rm h}(\tau_{\rm h}) = 1$. As shown in Fig. 3 of the main paper, both μ and $\tau_{\rm h}$ depend on φ. In particular, $\tau_{\rm h}$ is roughly an exponential function of φ

$$\tau_{\rm h} \sim e^{\alpha\varphi}, \tag{C4}$$

which suggests that there is no diverging density for $\tau_{\rm h}$.

---

[1] L. Berthier, G. Biroli, J.-P. Bouchaud, L. Cipelletti, and W. van Saarloos, eds., *Dynamical Heterogeneities and Glasses* (Oxford University Press, 2011).
[2] E. Witten, Physics Today **37**, 38 (1980).
[3] S. Franz and G. Parisi, Phys. Rev. Lett. **79**, 2486 (1997).
[4] M. Mézard and G. Parisi, J. Phys.: Cond. Matt. **12**, 6655 (2000).
[5] J.-P. Bouchaud and G. Biroli, J. Chem. Phys. **121**, 7347 (2004).
[6] W. Götze, *Complex dynamics of glass-forming liquids: A mode-coupling theory*, vol. 143 (Oxford University Press, USA, 2009).

[7] L. Berthier and G. Biroli, Rev. Mod. Phys. **83**, 587 (2011).
[8] G. Parisi and F. Zamponi, Rev. Mod. Phys. **82**, 789 (2010).
[9] T. R. Kirkpatrick and P. G. Wolynes, Phys. Rev. A **35**, 3072 (1987).
[10] J. Kurchan, G. Parisi, and F. Zamponi, J. Stat. Mech. **2012**, P10012 (2012).
[11] P. Charbonneau, J. Kurchan, G. Parisi, P. Urbani, and F. Zamponi, Nat. Comm. **5**, 3725 (2014).
[12] T. R. Kirkpatrick, D. Thirumalai, and P. G. Wolynes, Phys. Rev. A **40**, 1045 (1989).
[13] P. G. Debenedetti and F. H. Stillinger, Nature **410**, 259 (2001).
[14] S. K. Kumar, G. Szamel, and J. F. Douglas, J. Chem. Phys. **124**, 214501 (2006).
[15] J. D. Eaves and D. R. Reichman, Proc. Nat. Acad. Sci. U. S. A. **106**, 15171 (2009).
[16] B. Charbonneau, P. Charbonneau, Y. Jin, G. Parisi, and F. Zamponi, J. Chem. Phys. **139**, 164502 (2013).
[17] G. Biroli and J.-P. Bouchaud, J. Phys.: Cond. Matt. **19**, 205101 (2007).
[18] S. Franz, G. Parisi, F. Ricci-Tersenghi, and T. Rizzo, Eur. Phys. J. E **34**, 1 (2011).
[19] S. Franz, H. Jacquin, G. Parisi, P. Urbani, and F. Zamponi, Proc. Nat. Acad. Sci. U.S.A. **109**, 18725 (2012).
[20] G. Biroli, C. Cammarota, G. Tarjus, and M. Tarzia, Phys. Rev. Lett. **112**, 175701 (2014).
[21] H. Osada, Probab. Theory Related Fields **112**, 53 (1998).
[22] R. Candelier, O. Dauchot, and G. Biroli, Phys. Rev. Lett. **102**, 088001 (2009).
[23] K. S. Schweizer and E. J. Saltzman, J. Chem. Phys. **119**, 1181 (2003).
[24] K. S. Schweizer, J. Chem. Phys. **123**, 244501 (2005).
[25] P. Chaudhuri, L. Berthier, and W. Kob, Phys. Rev. Lett. **99**, 060604 (2007).
[26] S. Mirigian and K. S. Schweizer, J. Phys. Chem. Lett. **4**, 3648 (2013).
[27] J. P. Garrahan and D. Chandler, Proc. Nat. Acad. Sci. U. S. A. **100**, 9710 (2003).
[28] R. Candelier, A. Widmer-Cooper, J. K. Kummerfeld, O. Dauchot, G. Biroli, P. Harrowell, and D. R. Reichman, Phys. Rev. Lett. **105**, 135702 (2010).
[29] A. S. Keys, L. O. Hedges, J. P. Garrahan, S. C. Glotzer, and D. Chandler, Phys. Rev. X **1**, 021013 (2011).
[30] H. Tanaka, T. Kawasaki, H. Shintani, and K. Watanabe, Nat. Mat. **9**, 324 (2010).
[31] X. Xia and P. G. Wolynes, Proc. Nat. Acad. Sci. **97**, 2990 (2001).
[32] S. M. Bhattacharrya, B. Bagchi, and P. G. Wolynes, Proc. Nat. Acad. Sci., U.S.A. **105**, 16077 (2008).
[33] (Wiley, 2012).
[34] J. Kurchan, G. Parisi, P. Urbani, and F. Zamponi, J. Phys. Chem. B **117**, 12979 (2013).
[35] P. Charbonneau, J. Kurchan, G. Parisi, P. Urbani, and F. Zamponi, JSTAT **in press** (2014).
[36] M. Mézard and G. Parisi, in *Structural Glasses and Supercooled Liquids: Theory, Experiment and Applications*, edited by P.G.Wolynes and V.Lubchenko (Wiley & Sons, 2012).
[37] M. Skoge, A. Donev, F. H. Stillinger, and S. Torquato, Phys. Rev. E **74**, 041127 (2006).
[38] P. Charbonneau, A. Ikeda, G. Parisi, and F. Zamponi, Phys. Rev. Lett. **107**, 185702 (2011).
[39] B. Charbonneau, P. Charbonneau, and G. Tarjus, J. Chem. Phys. **138**, 12A515 (2013).
[40] S. Sengupta, S. Karmakar, C. Dasgupta, and S. Sastry, J. Chem. Phys. **138**, 12A548 (2013).
[41] P. Charbonneau, A. Ikeda, G. Parisi, and F. Zamponi, Proc. Nat. Acad. Sci. U. S. A. **109**, 13939 (2012).
[42] M. Mézard and A. Montanari, J. Stat. Phys. **124**, 1317 (2006).
[43] R. Mari, F. Krzakala, and J. Kurchan, Phys. Rev. Lett. **103**, 025701 (2009).
[44] R. Mari and J. Kurchan, J. Chem. Phys. **135**, 124504 (2011).
[45] M. Mézard, G. Parisi, M. Tarzia, and F. Zamponi, J. Stat. Mech. **2011**, P03002 (2011).
[46] H. L. Frisch and J. K. Percus, Phys. Rev. E **60**, 2942 (1999).
[47] F. Krzakala and L. Zdeborová, Phys. Rev. Lett. **102**, 238701 (2009).
[48] A. Ikeda, L. Berthier, and G. Biroli, J. Chem. Phys. **138**, 12A507 (2013).
[49] W. T. Elam, A. R. Kerstein, and J. J. Rehr, Phys. Rev. Lett. **52**, 1516 (1984).
[50] S. C. van der Marck, Phys. Rev. Lett. **77**, 1785 (1996).
[51] J. Helfferich, F. Ziebert, S. Frey, H. Meyer, J. Farago, A. Blumen, and J. Baschnagel, Phys. Rev. E **89**, 042603 (2014), URL `http://link.aps.org/doi/10.1103/PhysRevE.89.042603`.
[52] D. Stauffer and A. Aharony, *Introduction to Percolation Theory* (Taylor and Francis, Philadelphia, 1994).
[53] F. Höfling, T. Franosch, and E. Frey, Phys. Rev. Lett. **96**, 165901 (2006).
[54] K. Vollmayr-Lee, W. Kob, J.-L. Binder, and A. Zippelius, J. Chem. Phys. **116**, 5158 (2002).
[55] E. Flenner, H. Staley, and G. Szamel, `arXiv.org:1310.1029` (2013).
[56] G. M. Hocky, L. Berthier, W. Kob, and D. R. Reichman, `arXiv.org:1402.5974` (2014).
[57] L. O. Hedges, L. Maibaum, D. Chandler, and J. P. Garrahan, J. Chem. Phys. **127**, 211101 (2007).
[58] P. Mayer, K. Miyazaki, and D. R. Reichman, Phys. Rev. Lett. **97**, 095702 (2006), 0031-9007.
[59] J. J. Arenzon, A. Coniglio, A. Fierro, and M. Sellitto, `arXiv:1402.7003` (2014).
[60] K. Zhang, W. W. Smith, M. Wang, Y. Liu, J. Schroers, M. D. Shattuck, and C. S. O'Hern, cond-mat p. 1404.0465 (2014).
[61] M. Mézard, G. Parisi, and M. A. Virasoro, *Spin glass theory and beyond* (World Scientific, Singapore, 1987).
[62] T. Castellani and A. Cavagna, Journal of Statistical Mechanics: Theory and Experiment **2005**, P05012 (2005).
[63] D. Frenkel and B. Smit, *Understanding Molecular Simulation*, vol. 1 of *Computational Science Series* (Academic Press, San Diego, 2002).
[64] E. Flenner and G. Szamel, The Journal of Chemical Physics **138**, 12A523 (2013).
[65] E. J. Saltzman, G. Yatsenko, and K. S. Schweizer, J. Phys.: Condens, Matt, **20**, 244129 (2008).
[66] L. Berthier and D. Coslovich, ArXiv e-prints (2014), 1401.5260.

[67] L. Berthier, H. Jacquin, and F. Zamponi, Phys. Rev. E **84**, 051103 (2011).
[68] M. Mézard and A. Montanari, *Information, Physics and Computation* (Oxford University Press, 2009).
[69] G. Parisi and T. Rizzo, Phys. Rev. E **87**, 012101 (2013).
[70] A. R. Kerstein, Journal of Physics A: Mathematical and General **16**, 3071 (1983).
[71] S. C. van der Marck, Phys. Rev. Lett. **77**, 1785 (1996).
[72] C. B. Barber, D. P. Dobkin, and H. Huhdanpaa, ACM TRANSACTIONS ON MATHEMATICAL SOFTWARE **22**, 469 (1996).
[73] M. D. Rintoul and S. Torquato, Journal of Physics A: Mathematical and General **30**, L585 (1997).
[74] W. T. Elam, A. R. Kerstein, and J. J. Rehr, Phys. Rev. Lett. **52**, 1516 (1984).
[75] D. Stauffer and A. Aharony, *An Introduction to Percolation Theory* (Taylor and Francis, London, 1994), 2nd ed.